Earth and Planetary Science Letters https://doi.org/10.1016/j.epsl.2019.115867

The lifecycle of mid-ocean ridge seamounts and their prodigious flank collapses

J.E. Hunt[1]* and I. Jarvis[2]

[1] *National Oceanography Centre, Waterfront Campus, University of Southampton, European Way, Southampton, SO14 3ZH UK, james.hunt@noc.ac.uk*

[2] *Department of Geography and Geology, Kingston University London, Kingston upon Thames, KT1 2EE UK, i.jarvis@kingston.ac.uk*

Abstract

Volcanic seamounts are spectacular bathymetric features representing 'undersea mountains' comparable in size to volcanic islands. They are often sites of active volcanism, represent major marine habitats, and contain potentially globally significant commodities of trace metals. However, we know comparatively little about how they form, the extent of their volcanic lifecycle, and what risks they pose from periodic flank collapse. Here, we study a uniquely extensive 43 Myr record of volcaniclastic and calciclastic turbidites accumulated on the Madeira Abyssal Plain in the NE Atlantic, which originate from large submarine landslides from the adjacent Great Meteor-Cruiser seamount complex on the flanks of the Mid-Atlantic Ridge. These turbidites present the first long-term temporal record of the recurrence, magnitude, and emplacement mechanism of seamount flank collapses from a single seamount complex throughout its lifecycle. Landslides from the Great Meteor-Cruiser seamount complex are comparable size to those from the Canary Islands, with average volumes of 30-40 km^3 but can be as large as 130 km^3, comparable to many volcanic island landslides. These seamount landslides were predominantly multi-stage failures similar to those form neighbouring volcanic islands, but in contrast occurred preferentially during sea-level lowstands. We show that volcanic seamounts above mantle plumes have long protracted lifecycles, and that substantial flank failures are capable of occurring at all stages of development. Temporal change in turbidite composition has, for the first time, enabled reconstruction of the inception (around 43-45 Myrs ago), ascension (taking around 20-25 Myrs), emergence (after 30 Myrs) and later recession (last 9 Myrs), cessation in volcanism (last 4 Myrs) and subsidence of the seamounts (from 2 Myrs onwards). These seamounts above a mantle plume have taken around 26 Myrs to emergence above sea level from inception, while their volcanic island contemporaries only took 2-to-5 Myrs. Here, we use the history of turbidites derived from landslides from the seamounts to show how the seamounts developed and suffered mass wasting during their life cycles.

1. Introduction

There are more than 33,400 seamounts with seafloor elevations over 1,000 m and more than 138,400 with elevations 500–1,000 m, which combined globally represent 21% of the seafloor (Wessel et al. 2010; Yesson et al. 2011). Seamounts can be both volcanic, representing either submarine peaked volcanoes or flat-topped submerged and eroded volcanic ocean islands, or non-volcanic, representing ridges associated with transform or thrust faults (Schmidt & Schmincke, 2000; Palmiotto et al., 2013, 2017). Here, we focus on volcanic seamounts, which represent either active or extinct undersea volcanoes that commonly develop above intraplate plume bodies in association with mid-ocean ridge volcanism, or in association with volcanism above collision plate boundaries (Wessel et al. 2010; Yesson et al. 2011). Whilst many exhibit a conical shape and a relatively flat summit of limited area, seamount shape can be variable and is controlled by several characteristics: (1) size, geometry and migration of magma conduits; (2) eruption rates and viscosity of magmas; (3) crater or caldera development; (4) basement topography; and (5) regional gravitational stress (Schmidt & Schmincke, 2000). Volcanic seamount morphologies exist between two end-members depending principally on the geometry of the magma conduits: (1) point–source whereby magma is extruded from a single central vent; and (2) linear–source where magma is effused along ridges (Schmidt & Schmincke, 2000).

Basalts and andesites recovered from seamounts demonstrate long multimillion-year lifecycles (Batiza & Vanko, 1983; Honda et al. 1987; Pringle et al. 1991). Previous work has studied the geomorphology of seamounts thought to represent different stages of development (Vogt & Smoot, 1984; Chaytor et al. 2007; Mitchell & Lofi 2008; Dziak & Merle, 2016). These multibeam surveys suggest that seamounts develop irregular morphologies as a result of progressive slope failures that may occur long after volcanic activity ceases (Chaytor et al. 2007). These slope failures are assumed to be small-scale and infrequent, reflecting low time-averaged erosion rates (Chaytor et al. 2007; Mitchell & Lofi 2008; Dziak & Merle, 2016). However, despite the prevalence and importance of seamounts, their size, and

previous (albeit sparing) identification of flank failures, there is a significant gap in our understanding of seamount growth and denudation. Whilst much is now known about ocean island growth and collapse, little is known about the overall lifecycle of seamounts and their mass wasting. Specifically, little is known about the true scale, timing and frequency of submarine landslides on seamount flanks, and how mass wasting correlates to volcanic activity or the broader seamount life cycle.

Exceptionally large submarine landslides have previously been identified during subaerial shield-building and central edifice growth of volcanic islands (Carracedo, 1999; Hunt et al. 2013a). These prodigious mass movements often exceed 300 km^3, such as those in the Hawaiian, Canarian and Madeira archipelagos (Moore et al. 1989, 1994; Masson et al. 2002; Quartau et al. 2018). Submarine landslides of equal or greater magnitude also occur during the submerged seamount-stage of growth as volcanic islands undergo inception, ascension, and finally emergence above sea-level (Hunt and Jarvis, 2017). With submarine summit heights up to 5.5 km above the seafloor and bases up to 85 km wide, volcanic seamounts are comparable in dimension to ocean-island volcanoes, and are often many times larger than terrestrial volcanoes (Mitchell et al. 2003; Yesson et al. 2011). However, despite landslide scars and debris aprons identified on seamounts (e.g. Mitchell et al. 2003; Yesson et al. 2011), there is a lack of long-term geological records of landslides from seamounts.

Landslides linked to rapid growth of volcanic edifices, such as in the Canary or Hawaiian Islands, present a risk from tsunamigenesis. Although potentially grown at slower rates (Tucholke and Smoot, 1990), seamounts have high abundance across the seafloor, comprise steep slopes rising thousands of metres above the sea floor, and possess evidence of past mass wasting. Seamounts are also sites of oceanographic and biomass importance. They represent fragile ecosystems with a mixture of rocky seafloor exposure and mixed hard, firm and soft substrates within deep-water, middle-depth and shallow-water levels (Fock et al. 2002; Rogers, 2004; Morato et al. 2013). They are also nutrient upwelling sites, support large biomasses, have prolific benthic infaunal and epifaunal habitats, and represent important

marine mammal and fish breeding grounds, predatory feeding grounds, and migratory waypoints (Koslow, 1997; Holland et al. 2007; Kaschner, 2007; Clark et al. 2010). Seamounts also represent sites of important fluid, heat and solute fluxes, and provide important repositories of metals and rare-earth elements crucial for growing high-end technologies (Mitchell et al. 2003; Etnoyer et al. 2010; Fisher & Wheat, 2010; Hein et al. 2010; Staudigel & Clague, 2010). Better understanding seamounts is emphasised considering the rapid technological advances towards deep-sea mining exploiting seamounts as repositories of rare metals (Hein et al. 2010; Boschen et al. 2013). Understanding the growth and mass wasting processes in such areas is critically important for planning the maintenance of these ecosystems, identifying potential hazards, and for sustainably exploiting their resources (De Mol et al. 2008; Omira et al. 2016).

Despite volcanic seamounts being among the most abundant type of volcano, they represent the least explored physiographic feature on the Earth's surface and much of their lifecycle is theorised. Indeed, less than one percent of seamounts have been studied in any detail (Stuadigel & Koppers, 2015). Therefore, studies that elucidate processes at seamounts across their life cycle are important. This study provides a unique 43 Myr continuous record of distal turbidites in the Madeira Abyssal Plain, offshore NW Africa, which includes those from landslides on the adjacent Great Meteor-Cruiser Seamount Complex. The ages and volumes of these turbidites will provide a temporal record of mass wasting on the Great Meteor-Cruiser Seamount Complex, while temporal trends in their compositions may provide information on how the seamounts have developed over time. Indeed, resolving the life cycle of the Great Meteor-Cruiser Seamount Complex and its mass wasting can be compared to similar studies of the Canary Islands to provide further insights into volcano dynamics above mantle plumes and their instabilities (Hunt et al. 2014; Hunt & Jarvis, 2017). Our study aims to answer several key questions regarding the life cycle of seamounts and their susceptibility to flank collapses:

What is the magnitude and recurrence rate of flank collapses from seamounts?

Does mass wasting occur throughout the lifecycle of a seamount and do slide recurrence rates change through the lifecycle?

Can the composition of the mass wasting materials provide information on the development of seamounts during their lifecycle?

What processes precondition (and potentially trigger) flank collapses?

Do the slides occur as single failures or as multistage collapses?

2. Geology of the Great Meteor-Cruiser Complex

The Great Meteor-Cruiser Seamount Complex between 29ºN and 33ºN forms the southern component of the larger Atlantis-Meteor Complex adjacent to the western Madeira Abyssal Plain, offshore NW Africa. The Atlantis-Meteor Complex represents a north–south trending series of seamounts extending southwards from the Azores along the Mid-Atlantic Ridge towards the Madeira Rise (Fig. 1). These seamounts are thought to have formed above the New England hotspot with volcanic activity over the last 43 Myr and as recently as 3 Myr ago (Tucholke & Smoot, 1990). The Great Meteor and Cruiser seamounts individually represent the largest submarine edifices within this complex, and are also among the largest seamounts globally. With heights of over 4,500 m above the seafloor and summit areas greater than 1,465 km^2 they are dwarfed only by the seamounts of the Hawaiian-Emperor seamount chain.

The Madeira Abyssal Plain represents a large deep-sea depocentre between the Canary Islands and the mid-ocean ridge adjacent to the Great Meteor-Cruiser Seamount Complex from 35° to 26°N (Fig. 1). Here, turbidites accumulate from large-volume landslides from the continental slopes of NW Africa (NW Morocco, Western Sahara and Mauritania), the Canary Islands, and from the adjacent seamounts (Fig. 1). The colour, physical properties, petrology, and geochemical composition have previously been used to discriminate the distinct provenance of individual turbidites (de Lange et al. 1987; Weaver et al. 1992, 1998; Pearce

and Jarvis, 1992; Wynn et al. 2002; Hunt et al. 2014; Clare et al. 2014; Hunt and Jarvis, 2017). Here, we study 340-to-415 m-long ODP Cores (from Sites 950–952) recovered from water depths greater than 5,300 m in the central Madeira Abyssal Plain that provide a 43 Myr (middle Eocene-to-present) turbidite record of landslide activity (Fig. 1). The turbidites generally pond towards the basin centre and thin gradually towards the basin margins (Supplement 7; Weaver et al. 1992).

Previous work has highlighted the presence of different types of calciclastic turbidites in the basin stratigraphy and suggest they represent landslides from the Great Meteor-Cruiser Seamount Complex adjacent to the Madeira Abyssal Plain (Fig. 2) (de Lange et al. 1987; Weaver et al. 1992; Jarvis et al. 1998; Weaver et al. 1998; Hunt and Jarvis, 2017), including: dark-grey to black (basaltic) volcaniclastic turbidites older than 17 Ma (latest early Miocene), brown calciclastic (calcite-poor) turbidites, and white calciclastic (calcite-rich) turbidites, in addition to tephras older than 17 Ma (Jarvis et al. 1998). These deposits represent an as of yet undocumented natural archive of the growth and denudation of the Great Meteor-Cruiser Seamount Complex. We aim to study these deposits to elucidate where, when, how, and why these flank failures occurred at these seamounts.

3. Methods

3.1 Discriminating seamount flank collapses in the turbidite record

It is essential to distinguish between fine-grained sediment deposited by hemipelagic fallout (hemipelagite), representing dateable background sedimentation, and discrete turbidites associated with mass wasting on the seamounts (Table 1, Hunt et al. 2013a, 2014; Hunt & Jarvis, 2017). It is also important that turbidites only sourced from Great Meteor and Cruiser seamount landslides are studied, rather than those from the Canary Islands. Previous work has discriminated turbidites sourced from subaerial and submarine flanks collapses on the Canary Islands based upon their geochemical composition (Hunt et al. 2014; Hunt & Jarvis,

2017). Here, for the first time, we extract the seamount-sourced turbidites from the 43 Myr sedimentary record in the Madeira Abyssal Plain.

There are two principal types of calciclastic turbidites in the Madeira Abyssal Plain that represent the majority of seamount-sourced landslides (e.g. Fig. 1 and Supplements 1–3): (1) white calciclastic turbidites; and (2) brown calciclastic turbidite (Fig. 2, Table 1, Supplements 1–3; Jarvis et al. 1998). The geochemical composition of these calciclastic turbidites has previously excluded them from either submarine or subaerial landslides on the Canary Islands and Madeira (Hunt et al. 2014; Hunt & Jarvis, 2017). Although isolated deposits occur immediately adjacent to the Selvagen Islands in Agadir Basin, previous work suggests that sediments from here are restricted to the Agadir Basin (Wynn et al. 2002; Hunt et al. 2013c; Santos et al. 2019).

Black volcaniclastic turbidites of middle-Eocene-age are present and likely represent failures of early eruptive materials exposed on the flanks of seamounts adjacent to the Madeira Abyssal Plain (Supplement 3; Jarvis et al. 1998; Weaver et al. 1998). There are also thin-bedded tephra deposits restricted to the record older than 18 Ma (Supplements 1–3). There are no tephras in the 17 Ma-to-present Madeira Abyssal Plain stratigraphy, despite known eruptions in the Canary Islands recorded at ODP Sites proximal to the Western Canary Islands (Weaver et al. 1992; Rodehorst et al. 1998; Hunt et al. 2014). Tephras older than 18 Ma are unlikely to represent Canary Island eruptions but rather near-by underwater eruptions at adjacent seamounts; furthermore only the easternmost Canary Islands existed during this time, and were themselves in the early stages of development (van den Bogaard, 2013; Hunt & Jarvis, 2017).

3.2 Stratigraphy and age dating of turbidites

The 17 Ma-to-present stratigraphy of the Madeira Abyssal Plain was previously constructed based upon three ODP Sites (950–952) (Hunt et al. 2014; Clare et al. 2014). Here, this

stratigraphy has been extended to 43 Ma at ODP Site 950 (Supplement 3). Individual turbidites were dated using an age-model based on established coccolith biostratigraphy, magnetostratigraphy and lithostratigraphy of the hemipelagite sediment in which they are emplaced (Supplement 4; Howe and Sblendorio-Levy, 1998; Hunt et al. 2013a, 2014; Hunt and Jarvis, 2017).

Coccolith biostratigraphy and magnetostratigraphy have previously been used to construct a robust age-model for dating turbidites in the Madeira Abyssal Plain for the last 17 Myrs, this is extended here to 43 Myr (Supplement 4; Weaver & Kuijpers, 1983; Hunt et al., 2013a, 2013c, 2014). Coccolith biostratigraphy provided down-core datum horizons based primarily on first and last occurrences (Supplement 4; Howe and Sblendorio-Levy, 1998; Hunt et al. 2013a, 2013c, 2014). Magnetostratigraphy provides down-core datum horizons based on established excursions in magnetic polarity or intensity (Howe and Sblendorio-Levy, 1998). The hemipelagite lithostratigraphy has been used to refine this age model for the last 5.4 Myr (Supplement 4; Hunt & Jarvis, 2017). Hemipelagite lithology varies between interglacial coccolith-rich white carbonate ooze and glacial carbonate-poor red-brown clay (Fig. 2, Supplement 1-2; Weaver & Kuijpers, 1983; Hunt et al., 2013a, 2013c, 2014; Hunt & Jarvis, 2017). Boundaries between interglacial and glacial hemipelagite lithologies have successfully been linked to Marine Isotope Stage boundaries, providing another source of dating (Hunt & Jarvis, 2017). The ages of the turbidites beds within the Madeira Abyssal Plain stratigraphy have uncertainties of ±10 ka conservatively in the last 5.4 Myr and to within 1-5% of the age in the strata older than 7.0 Ma, but have been refined further in recent works (e.g. Hunt and Jarvis, 2017).

3.3 Geochemical compositions of calciclastic turbidites

The compositions of the calciclastic turbidites may reveal insights into their precise provenance from the seamounts. Differences in geochemical composition may reflect failure

of materials at different depths on the seamounts, during different phases of volcanism, or represent different periods of sediment retention on the seamount slopes before mass wasting. Temporal variations in turbidite geochemical compositions may reflect different stages of seamount development. The geochemical compositions of these beds were derived from published bulk geochemistry determined by ICP-AES and ICP-MS (Jarvis et al. 1998); following the methods of Totland et al. (1992) and Jarvis (2003). Here, we re-analyse compositional data of turbidite mudcaps utilising diagnostic geochemical properties previously identified as capable of resolving the provenance of turbidites offshore NW Africa (Fig. 3, Table 2; Croudace et al. 2006; Hunt et al., 2014, 2015a, 2015b; Hunt & Jarvis 2017).

3.4 Slide magnitudes based on turbidite volume calculations

The volume of the turbidites, and the slides by association, are derived using the methodology of Hunt *et al.* (2014) and Hunt and Jarvis (2017), based on the method of Weaver (2003), using the seismic interval and decompacted volumes from Rothwell *et al*. (1998). An expanded methodology is detailed in supplement 5-9, which involves taking the decompacted thickness of turbidites from the ODP Cores and comparing to the decompacted thickness of seismic packages mapped across the Madeira Abyssal Plain, and their decompacted volumes.

3.5 Statistics of bed recurrence and correlation to sea-level state

Statistical analysis of the recurrence of the calciclastic beds representing seamount flank failures followed the methods of Hunt *et al*. (2014) and Clare *et al.* (2014, 2016). The recurrence periods of these turbidites were analysed on probability of exceedance plots. Probability of exceedance plots of the recurrence time between the specific brown and white calciclastic turbidites may provide insights into type of process(s) controlling recurrence. Exponential distributions on log–log plots suggest the influence of a Poissonian, or otherwise

random, control. Linear distributions of recurrence may indicate events of common recurrence and imply a non-random control (Clare et al. 2014, 2016). The Hurst exponent (*K*) is used to identify clustering and whether there is trend-reinforcement. *K*=0.5–0.6 indicates no significant trend-reinforcement, which implies a likely randomly or non-clustered distribution with respect to preceding or succeeding events, and suggests that a control on the distribution is unlikely to be a cyclical or rhythmic process.

3.6 Identification of sub-units within beds

Visual interrogation of the split cores showed multiple fining-upwards patterns within individual beds, and allowed the identification of sub-units and inference of multistage failure. Distinct oxidation fronts (cf. Thomson *et al*., 1998) were also visible and discounted from inclusion when identifying sub-units. High-resolution images of ODP Core 950, 951 and 952 were obtained through the ODP *Janus* database. Down-core greyscale features extracted from high-resolution images of the turbidites using *ImageJ* supported visual inspection of sub-units, following the methods of Hunt and Jarvis (2017). To remove artefacts in this process, such as bioturbation, adjacent down-core profiles were constructed every ten horizontal pixels and then averaged to give a down-core greyscale profile. Excursions in grey-scale towards darker values highlighted the presence of volcanic silts representing the bases of sub-units.

4. Results and Discussion

4.1 Integrating flank collapse history and seamount lifecycle

This serves to combine results and discussion of the questions related to the: (1) magnitude and recurrence of flank collapses from seamounts; (2) presence of changes in mass wasting recurrence throughout the lifecycle of a seamount; and (3) whether turbidite compositions can provide information about the lifecycle development of seamounts.

4.1.1 Inception and early flank failures

The oldest middle-Eocene (~43 Ma) turbidites in the Madeira Abyssal Plain are metre-thick, normally graded, medium-to-very coarse basaltic sands (250–2000 μm) that occur in association with tephras (Supplement 3). Turbidites sourced from the Canary Islands contain only coarse-silt to very fine-sand grade material in the bases (100–150 μm) (Hunt et al. 2013a, 2013b). Here, these coarser-grained turbidites have a more proximal provenance, likely from the adjacent seamounts; while volcanic islands further afield that have yielded much finer-grained sediment (Hunt et al. 2013a, 2014; Hunt & Jarvis, 2017). Additional basaltic, volcaniclastic, sand-rich turbidites occur in three clusters in the latest middle Eocene to late Oligocene at 39–35 Ma, 33.5–30 Ma, and 28.4–27.7 Ma (Supplement 3), where landslides occurred at frequencies of 4-to-7 per million years during these periods. These clusters also include brown calciclastic turbidites and tephras, and each cluster has a decimetre-thick white calciclastic turbidite present towards the top (Supplement 3).

We suggest that the coarse-grained volcaniclastic sands at ~43 Ma likely represent failure (10–30 km^3) of voluminous extruded basalts and hyaloclastites associated with the inception of seamounts in the Great Meteor-Cruiser Seamount Complex (Supplement 3). A later Eocene 39–35 Ma cluster of volcaniclastic sands specifically represents inception of the Cruiser Seamount, as these and associated tephras are similar in age to the estimated 37 Ma maximum age of the seamount (Tucholke & Smoot, 1990). Brown calciclastic turbidites occur during this period, typified by laminated silts and cm–dm-thick mudcaps. These likely represent failure (10–30 km^3) of the developing submarine edifice flanks draped in carbonate-poor pelagites accumulating below the ACD and calcite lysocline but above the CCD. They may represent failures as the seafloor deformed in response to initial magma ascent and later rift-arm activity. There is a white calciclastic turbidite at 35.5 Ma atop this sequence that is represented by a carbonate-rich, fine-grained and structureless mudcap (Supplement 3). This

bed likely demonstrates that the Cruiser seamount had grown above the ACD by the late Eocene that enabled sedimentation and preservation of carbonate-rich pelagites that later failed to form this deposit.

This pattern of turbidites is repeated in the early Oligocene (33.5-30 Ma), coincident with the initiation and growth of the Great Meteor seamount, which has a maximum age estimate of 33 Ma (Fig. 4) (Tucholke & Smoot, 1990). We suggest that prior to 32.2 Ma, edifice growth deformed and destabilised the seafloor resulting in brown calciclastic turbidites. We suggest voluminous extrusive volcanic growth superseded this, with deep-seated failures resulting in basalt-rich volcaniclastic landslides. Pelagite drapes developed on the edifice while below the lysocline and later failed, depositing further brown calciclastic turbidites until 30.2 Ma. After this, the seamount rose above the lysocline and ACD, enabling the deposition and preservation of carbonate-rich pelagites that later failed and produced white calciclastic turbidites (Supplement 3). The brown and white calciclastic turbidites result from relatively shallow-seated but aerially extensive failures of predominantly hemipelagite-rich sediment. A shorter period characterised by this pattern of beds occurred in the mid-Oligocene between 28.4 and 27.7 Ma (Supplement 3), and may represent formation of another adjacent seamount or contemporary edifice (Tucholke & Smoot, 1990).

4.1.2 Vertical ascension of seamounts and flank collapse

In the late Oligocene to early Miocene, during the intervals 26.5–24.3 Ma, 23–20 Ma and ~18 Ma, black volcaniclastic turbidites were replaced in the stratigraphy by thin pale-grey 'non-volcaniclastic' turbidites (Supplement 3). These particular pale-grey 'non-volcaniclastic' turbidites have been suggested to originate from mass wasting adjacent to Fuerteventura and Lanzarote in the Canary Islands during inception (Hunt and Jarvis, 2017). Alternatively, the association of these beds with the brown calciclastic beds and later white calciclastic beds suggest they represent 10–30 km^3 failures of the flanks of the Great Meteor and Cruiser

seamounts during early vertical growth, or represent inception and growth of the additional seamounts to the west of the Madeira Abyssal Plain, for example Little Meteor, Plato, Irving and Hyeres seamounts (Supplement 3; Tucholke and Smoot, 1990). Unlike the black volcaniclastic turbidites, we suggest these pale-grey 'non-volcaniclastic' turbidites represent more shallow-seated but aerially expansive failures. Compared to the previous period of flank failures during seamount inception, these slides occurred during seamount ascension with slide frequency fell from 4–7 per million years to 2–3 per million years.

4.1.3 Giant flank collapses of the Great Meteor-Cruiser Seamount Complex

Early-Miocene beds deposited between 16.5 and 16 Ma include metre-thick, white, calciclastic, sand-rich turbidites (calcarenites) recovered at all three ODP Sites (Fig. 2, Supplement 3). These carbonate sands include abundant shallow-water benthic foraminifera (e.g. *Amphistegina* sp.), which implies an origin from failure of thick carbonate-rich hemipelagite drapes accumulated in shallow water depths <130 m where there was significant benthic carbonate production (Murray, 1990). These decimetre-to-metre-thick calcarenites (up to 10.5 m thick) comprise sand-sized calcareous debris with a high neritic bioclastic component, unaltered volcaniclastic debris (including basaltic fragments, glass shards and ferromagnetic mineral assemblages), and large granule-to-pebble sized red clay clasts. The beds are normally-graded but structureless, implying deposition from coarse-grained turbidity currents that deposited sediment rapidly, such that sediment was not reworked (e.g. Fig. 2). The abundance of coarse-grained, rounded and abraded shallow-water bioclastic carbonate clasts implies that the slopes that failed were subject to wave reworking in shallow <15–40 m water depths. Thus the edifice was at or emergent above sea-level. These coarse turbidite sediments suggest a close proximity to source, which supports a provenance from the Great Meteor-Cruiser Seamount Complex (maximum 130 km away) rather than the Canary Islands (>650 km away). Coarse, vesicular, altered volcaniclastic glasses are present and imply

residence on the seamount slopes for significant periods before being redeposited (Jarvis et al. 1998; Hunt et al. 2011).

Volcanic rocks recovered from the Great Meteor seamount date volcanism between 16.9 and 15.8 Ma (Wendt et al. 1976). Thus these turbidites at this time may represent failures from a shallow carbonate shelf around the Great Meteor seamount whereby volcanism preconditioned and potentially triggered flank failure. The thickest individual calcarenite deposits (up to 1.1 m; Schminke et al. 1995) occur at Site 950 located in a fracture zone equidistant between the Cruiser and Great Meteor seamounts. While different numbers of thinner, graded and un-graded calciclastic sand-rich turbidites were recovered at Sites 951 (to the NE) and 952 (to the SE) each site has numerous calcarenite beds. It is likely that both the Great Meteor and Cruiser seamounts incurred flank collapse during this episode. These large (50–250 km^3, combined up to 840 km^3) collapses represent flank collapses during peak elevation of the seamounts whilst at or emergent above sea-level. These slides may have failed between 1,000 and 3,200 km^2 of shallow seamount slope, producing failures of 30 to 250 m-thick blocks. However, the compositions of these turbidites implicate these slides were likely shallow-seated with large aerial extensive extents. Original volumes were likely smaller, as turbidite volumes are likely elevated by up to 50% by seafloor erosion *en-route* to the basin (Hunt, 2018). Sparse examples support these large volumes where seamount landslide volumes elsewhere can be up to 500 km^3, albeit requiring much deeper-seated failures (Omira et al. 2016).

Here, these seamounts that developed above a mantle plume took almost 26 Ma to grow and become emergent above sea level before finally subsiding. This is in contrast to neighbouring volcanic islands of the Canarian archipelago that grew more rapidly and only took between 2 and 5 Myrs to become emergent following inception (Hunt & Jarvis, 2017).

4.1.4 Flank collapses during continued stable growth

The frequency of white and brown calciclastic turbidites (10-80 and 10–30 km^3, respectively) increased in the middle-Miocene (Fig. 4, Table 2). From 16 to 12 Ma the geochemical compositions of the turbidite mudcaps are relatively constant, albeit with decreasing concentrations of SiO_2, otherwise indicating that the seamounts where most likely stable, neither growing significantly nor subsiding. From around 12 Ma there is a significant increase in both the frequency and volume of slides (Figs 4–5), which is thought to be coeval with a change in the rate of volcanic growth of the seamounts, indicated by an increase in Fe_2O_3 contents of the white and brown calciclastic turbidites, representing increased volcanic material present in failed masses. These suggest that widespread basaltic volcanism likely increased rapidly at both shallow central edifice and deep lateral rift locations between 12 and 9.5 Ma. Widespread basaltic volcanism ceased at central edifice sites at 9.5 Ma and focussed at the deeper lateral rifts on the submarine flanks from 8 to 4 Ma (Fig. 4). This is indicated by a continued increase in Fe_2O_3 (signifying volcaniclastic input) in brown calciclastic turbidites sourced from failures beneath the lysocline on the rift arms between 8 and 4 Ma, whilst Fe_2O_3 and TiO_2 decline in white calciclastic turbidites at 9.5 Ma, representing flank failure above the lysocline from the central edifice (Fig. 5, Table 2).

In the latest Miocene at 6.0 Ma there was a marked increase in the frequency to as many as 5-12 per million years, and an increase in thickness of white calciclastic turbidites from the shallower-water flanks of the seamounts (Fig. 4, Table 2). Increases in Sr-rich aragonite in white calciclastic turbidites, which is reflected by the increased Sr and Sr/Ca contents, imply volcanic growth had resulted in vertical ascension of the seamounts back into shallower and warmer waters (Fig. 5, Table 2). At 6.0 Ma there is also an increase of Zr and Zr/Ti ratio in these turbidites reflecting increased delivery of terrestrial wind-blown sediment at these now shallow-water sites, with a reduced input of volcanic products. During this episode volcanism at the central edifice may have become increasingly potassic with marked increases in K_2O at 6.0 Ma (Figs 4–5, Table 2). These post-6.0 Ma flank failures are much larger than previous seamount flank failures, whereby each slide involves as much as 120 km^3.

4.1.5 Collapse of dormant edifices

Mid-Pliocene to early-Pleistocene turbidites deposited between 4.0 and 2.0 Ma have a decline in Fe_2O_3 contents, reflecting a gradual decrease in basaltic volcanism and availability of volcanic materials that could be incorporated into the slides (Fig. 5, Table 2). The elevation of the seamounts remained stable during this time, as there are constant Sr/Ca, Zr and K_2O compositions (Figs 4–5, Table 2). From 2.0 Ma onwards there is a decline in the frequency of white calciclastic turbidites and a complete absence of brown calciclastic turbidites (Figs 4–5, Table 2). The white calciclastic turbidites also decrease in TiO_2, Fe_2O_3 and K_2O contents at this time (Fig. 5). This may indicate a cessation in all volcanic activity on the seamounts, with failures of only purely pelagic sediment accumulations (Fig. 4). The gradual decrease in Sr/Ca and marked decrease in Sr in white calciclastic turbidites from 2.0 Ma onwards indicates the elevation of the seamounts may be decreasing towards deeper and colder water depths, which may be explained by thermal subsidence following cessation of volcanic activity (Figs 4–5, Table 2). The general size of carbonate-rich seamount flank collapses decreases during this period, although rare examples have maximum volumes of 160 km^3.

4.2 Preconditioning seamount flank collapses

From 43 to 26 Ma there was inception of the Great Meteor-Cruiser Seamount Complex with associated volcanism, which most likely both preconditioned (provision and over-steepening of materials) and triggered (ground accelerations) seamount flank collapses. Volcanic activity was also likely responsible for flank failures during seamount ascension from 26 to 16 Ma and stable growth from 16 to 6.0 Ma. The present study implies that volcanism on the Great Meteor-Cruiser Seamount Complex declined and ceased after 6.0 Ma, reducing its influence as a trigger. However, slope failures are present during this period, with similar magnitudes

and are more frequent. Preconditioning may be linked to more rapid hemipelagite accumulation on already over-steepened flanks in shallower water-depths or linked to fluid expulsion; however, the trigger for these failures is less clear.

Previous studies have dated Quaternary marine sediments in the Madeira Abyssal Plain with conservative age uncertainties in the last 1.5 Myr of ±10 kyr. Analysis of the hemipelagite lithostratigraphy in the Madeira Abyssal Plain has extended this relatively high level of age certainty to the last 5.4 Myr (Hunt and Jarvis, 2017). Coccolith biostratigraphy and magnetostratigraphy dating uncertainties of strata prior to 7.0 Ma is on average ±1–5% of the age, thus uncertainties range between 12 ka and 270 ka in the 43-to-7 Ma record (Howe and Sblendorio-Levy, 1998; Hunt and Jarvis, 2017).

From 17 to 2.0 Ma brown calciclastic turbidites occur in broad clusters on average 300 kyr-long that occur every ~1.7 Myr. In the stratigraphy older than 17 Ma, the same brown calciclastic turbidites occur in clusters every ~1.45 Myr that last on average 1.0 Myr. The regularity of these clusters and a Hurst exponent of K=0.41 (N=83) that indicates non-randomness to their recurrence. The Hurst exponent of K<0.5 shows that there is tendency of a bimodal recurrence that switches between low and high values, and that there is a prevalence of anti-persistency (Clare et al. 2014). This is to say that during this time series a trend towards decreasing recurrence is more likely followed by a trend of increasing recurrence time, and *vice versa*. This is supported by log-normal distribution for the probability of exceedance of recurrence intervals between these turbidites (Fig. 6).

Volcanism declined and ceased between 6.0 and 4.0 Ma, which implies that the slides previously triggered by volcanism may be triggered by an alternative mechanism during this period. There is reliable global sea-level data from 7.0 Ma-to-present (e.g. Miller et al. 2005); here, we compare the timing of slides to sea level change. During this time, 15 brown calciclastic beds (83% of these beds), which represent failures of the deeper rift flanks, occurred at the lowest points in sea-level of particular glacial-interglacial cycles (Fig. 6). The

aforementioned dating uncertainty (±10 ka) from the age-model decreases the strength in drawing a correlation to climate. However, these turbidites are predominantly deposited during accumulation of red hemipelagite clays associated with glacial or lowstand sea level states, which supports attribution of slides occurring during low sea-level. While this may implicate a potential influence of glacial-interglacial climate change, the recurrence time (1.45 to 1.7 Myr) between clusters is much greater than the periodicity of glacial-interglacial cyclicity.

The broad recurrence intervals and low Hurst exponent (K=0.41) of these brown calciclastic turbidites invokes anti-persistence controls and implies a process such as magmatism as the likely primary preconditioning factor. It has previously been suggested that the development of rift systems and associated dyke intrusion explain the triggering of many landslides from volcanic island edifices (Elmsworth and Voight, 1996; Elmsworth and Day, 1999; Mitchell, 2003). Time series analysis of seismicity during dome-forming eruptions found seismicity associated with magma ascent to be cyclical between high and low seismicity in a trend described as being anti-persistent (Currenti et al., 2005); similar to the anti-persistent pattern of recurrence in these seamount landslides.

The Great Meteor seamount and adjacent seamounts of the southern Atlantis-Meteor Complex were volcanically active as late as 18, 14, 11, 10 and 6 Ma, respectively; with the Great Meteor Seamount itself displaying activity between 33 and 11 Ma (Tucholke and Smoot, 1990). This includes specific volcanic events on the Great Meteor Seamount that have been dated at 16.4, 16.3, 16.2, 11.0, 10.7 and 9.7±0.5 Ma (Wendt et al. 1976). These dates are similar to periods of brown calciclastic turbidite deposition, implying that volcanism, specifically along rift arms in deep water, may precondition and/or trigger slides. These data suggest temporal distributions of brown calciclastic turbidites may be influenced by magmatic processes, while the role of sea-level remains unclear.

There are only nine white calciclastic beds older than 17 Ma, whereas there have been 75 beds deposited from 17 Ma to present. There is no distinct pattern to periods of landslide

activity, but periods lasted on average 1.25±0.15 Myr, which include: 16.5–16.0 Ma (noted for calcarenite-rich calciclastic turbidites), 14.6–13.5 Ma, 12.0–11.4 Ma, 10.8–9.5 Ma, 8.4–7.4 Ma, 6.4–5.2 Ma, 4.8–3.5 Ma, 2.5–1.1 Ma and <0.8 Ma, and are separated by periods of inactivity of between 0.3 Ma and 1.5 Ma. The Hurst exponent for the white calciclastic turbidites is K=0.52 (N=76), implicating a random time series where there is no linear dependency; whereby one event will not affect the occurrence of the next (Clare et al. 2014). Despite the Hurst exponent, the recurrence intervals (time since last slide) of these beds better fit a log-normal distribution on probability of exceedance plots (Fig. 6), which instead implies a non-random control to their recurrence. In the last seven million years, we discovered that 27 of the 43 white calciclastic turbidites (63%) occurred during the lowest point of sea-level within glacial or lowstand marine isotope stages. A further seven beds occur at distinct low sea-level periods in interglacial or otherwise highstand periods (16%), thus 79% in total occur during lowstands or periodic sea-level lows (Fig. 6). Although dating uncertainty with the age-model may decrease the strength in these correlations of slide recurrence to climate, the turbidites are deposited within red hemipelagite clays representing glacial or lowstands in sea-level.

Volcanic activity likely represents both preconditioning and eventual triggering of slides during the inception, ascension and emergence of seamounts. However, environmental conditions associated with low sea-level may influence preconditioning and triggering of slides when volcanism ceases and the seamount undergoes subsidence. A review of landslide heights on volcanic islands and seamounts shows a particular prevalence of seamount slides occurring at or immediately above sea-level, and suggests a potential influence of sea-level change on slope stability (Mitchell, 2003). Failure of seamount flanks preferentially during lowstands of sea-level contrasts with the prevalence of flank collapses on more rapidly constructed volcanic islands where slides occur more frequently during rising and high-stands of sea-level, e.g. Canary Islands (Hunt et al. 2013a, 2014; Hunt and Jarvis, 2017).

4.3 Multistage collapse of seamount flanks

The flank collapses from the Cruiser and Great Meteor seamounts involve on average 30–50 km^3 of calciclastic sediment, although these can be as large as 150 km^3; enough to cover the US State of Florida in 1 m of sediment. We suggest that these represent relatively shallow-seated but aerial extensive failures of seamount slopes. The slides specifically responsible for the white calciclastic turbidites represent failures that may have occurred over 5.5 km above the abyssal plain at either shallow water depths or during subaerial emergence of the seamount. Therefore, these slides posed potential tsunamigenic hazards.

Slide volume is the single largest control on tsunamigenesis (Murty, 2003). Although smaller in volume than contemporary volcanic island flank collapses, these seamount slides commonly involve at least 30 km^3 of sediment and occur on steep slopes several thousand meters above the seafloor. Therefore there is a need to identify whether they failed as a single slab slide or whether they failed in multiple stages, because the mechanism of failure controls the proportion of the total slide volume that is tsunamigenic at any one time (Giachetti et al. 2011; Hunt et al. 2011, 2013b).

The presence of multistage failure is identified by the pervasive presence of multiple fining-upwards turbidites, called sub-units, within a single event bed (Hunt et al. 2011, 2013a, 2013b). Many beds older than 7.0 Ma are only a few tens of centimetres thick. Nonetheless, around 70% of these beds have two or more sub-units. In the last 7.0 Myr there are 43 white calciclastic turbidites identified and correlated between ODP Sites, 19 were less than 10 cm thick (~10–30 km^3), of which 11 (58%) have confirmed two or more sub-units. In the same period, 22 of 24 white calciclastic beds (92%) between 20 and 180 cm-thick (up to 150 km^3) have two or more sub-units (Fig. 7). Multistage collapses are thus a common failure mechanism among seamount flank collapses in the Great Meteor-Cruiser Seamount chain, and serve to reduce the tsunamigenic potential of these slides. This suggests that multi-stage failures are a more ubiquitous process in large volume landslides from volcanic edifices above

mantle plumes, as multistage failures have also been discovered during different stages of volcanic island development in the Canary Islands (e.g. Hunt et al., 2011, 2013b, 2015b) and Hawaiian Islands (Garcia & Hull, 1994; Garcia, 1996).

5. Conclusion

Our study shows that seamounts are susceptible to large-volume submarine landslides throughout their life cycle, which can span more than 40 Myr. The Great Meteor-Cruiser Seamount Complex began to grow 43 Myr ago and took 26 Myr to become fully emergent, in contrast to the Canary Islands that took between 2 and 5 Myrs. We show that the Meteor-Cruiser Seamount Complex effectively became inactive in the last 4 Myr and is currently undergoing subsidence. The different lithofacies and geochemical compositions of the turbidites deposited from these slides have enabled the complete lifecycle of a seamount complex to be recreated, including inception, ascension, emergence, recession, volcanic cessation and final thermal subsidence (Fig. 4). We show that on average these seamounts incur a flank collapse every 120±20 kyr and each time fail on average 30–50 km^3 of sediment, although failures may be as large as 160 km^3. Despite the prodigious volumes involved in these failures, they are commonly multistage and thus have reduced tsunamigenic potential. We show that there are cyclical factors influencing flank collapse, and that magmatism may both precondition and trigger flank collapse. This study indicates that glacial conditions and sea-level lowstands may be conducive towards shallow flank collapse at seamounts, but there is too great uncertainty in age dating for a reliable diagnosis.

Understanding the history of seamount growth, development and subsidence, and stability of submarine flanks during the lifecycle indicate that seamounts possess geohazard potential. This information raises questions as to how mass wasting at these sites may affect important habitats and may influence upwelling or oceanographic currents by regularly modifying the seamount topography that ocean currents interact with. This information also highlights that

exploration and exploitation of seamounts for mineral reserves need to focus on sites with dormant or preferably extinct volcanic or hydrothermal systems, removing the potential of those processes that precondition or trigger flank collapse.

References

Alibes, B., Canals, M., Alonso, B., Lebreiro, S.M., Weaver, P.P.E., 1996. Quantification of Neogene and Quaternary sediment input to the Madeira Abyssal Plain, *Geogaceta*, 20, 2, 394-297.

Alibes, B., Rothwell, R.G., Canals, M., Weaver, P.P.E., 1999. Determining of sediment volumes, accumulation rates and turbidite emplacement frequencies on the Madeira Abyssal Plain (NE Atlantic): a correlation between seismic and borehole data. *Mar. Geol.*, 160, 3-4, 225-250.

Balsam, W.L., 1983. Carbonate dissolution on the Muir Seamount (western North Atlantic): interglacial/glacial changes. *J. Sed. Petrol.*, **53**, 719–731.

Batiza, R., Vanko, D., 1983. Volcanic development of small oceanic central volcanoes on the flanks of the East Pacific Rise inferred from narrow-beam echo-sounder surveys. *Mar. Geol.*, **54**, 53-90.

Berger, W.H., 1978. Deep-sea carbonate: pteropod distribution and the aragonite compensation depth. *Deep Sea Res.*, **25**, 447–452.

Boschen, R.E. Rowden, A.A., Clark, M.R., Gardner, J.P.A., 2013. Mining of deep-sea seafloor massive sulphides: A review of deposits, their benthic communities, impacts from mining, regulatory frameworks and management strategies. *Ocean Coast. Manage.*, **84**, 54-67.

Carracedo, J.C., 1999. Growth, structure, instability and collapse of Canarian volcanoes and comparisons with Hawaiian volcanoes. *J. Volcanol. Geotherm. Res.*, **94**, 1–19.

Castillo, S., Moreno, T., Querol, X., Alastuey, A., Cuevas, E., Herrmann, L., Mounkaila, M. and Gibbons, W., 2008. Trace element variation in size-fractionated African desert dusts. *J. Arid Environs.*, **72**, 6, 1034-1045.

Chaytor, J.D., Keller, R.A., Duncan, R.A., Dziak, R.P., 2007. Seamount morphology in the Bowie and Cobb hot spot trails, Gulf of Alaska. *Geochem. Geophys. Geosys.*, **8**, 9, 1-26.

Clare, M.A., Talling, P.J., Challenor, P., Malgesini, G., Hunt, J.E., 2014. Distal turbidites reveal a common distribution for large (>0.1 km^3) submarine landslide recurrence. *Geology*, **42**, 263–266.

Clare, M.A., Talling, P.J., Challenor, P.G., Hunt, J.E. 2016. Tempo and triggering of large submarine landslides: statistical analysis for hazard assessment, in: Lamarche, G. *et al*. (Eds.), *Submarine Mass Movements and their Consequences*, Advances in Natural and Technological Hazard Research, **41**, Springer, Switzerland, 509–517.

Clark, M.R., Rowden, A.A., Schlacher, T., Williams, A., Consalvey, M., Stocks, K.I., Rogers, A.D., O'Hara, T.D., White, M., Shank, T.M. Hall-Spencer, J.M., 2010. The ecology of seamounts: structure, function and human impacts. *Ann. Rev. Mar. Sci.*, **2**, 253–278.

Croudace, I.W., Rindby, A., Rothwell, R.G., 2006. ITAX: description and evaluation of a new multi-function X-ray core scanner, *Geol. Soc. London Spec. Pub.*, **267**, 51-63.

Currenti, G., Del Negro, C., Lapenna, V., Telesca, L., 2005. Scaling characteristics of local geomagnetic field and seismicity and their dynamics in relation to the eruption activity. *Earth Planet. Sci. Letts.*, **235**, 1-2, 96-106.

de Lange, G.J., Jarvis, I. and Kuijpers, A., 1987. Geochemical characteristics and provenance of late Quaternary sediments from the Madeira Abyssal Plain, N Atlantic. *Geol. Soc. London Spec. Pub*, ***31***, 1, 147-165.

De Mol, B., Huvenne, V., Canals, M., 2008. Cold-water coral banks and submarine landslides: a review. *Int. J. Earth Sci.*, ***98***, 885.

Duffield, W.A., Stieljes, L., Varet, J., 1982. Huge landslide blocks in the growth of Piton de la Fournaise, La Reunion, and Kilauea volcano, Hawaii. *J. Volcanol. Geotherm. Res.*, **12**, 147–160.

Dziak, R.P. and Merle, S.G., 2016. Growth, Demise, and Recent Eruption History of the Eastern Cobb-Eickelberg Seamounts at the Intersection with the Juan De Fuca Ridge, in: Duarte, J.C., Schellart, W.P. (Eds.), *Plate Boundaries and Natural Hazards*, Geophysical Monograph, **219**, 241-258.

Elsworth, D., Day, S.J., 1999. Flank collapse triggered by intrusion: the Canarian and Cape Verde Archipelagos. *J. Volcanol. Geotherm. Res.*, **94**, 323–340.

Elsworth, D., Voight, B., 1996. Evaluation of volcano flank instability triggered by dyke intrusion. *Geol. Soc. London Spec. Pub*, **110**, 45–54.

Etnoyer, P.J., Wood, J., Shirley, T.C., 2010. How large is the seamount biome? *Oceanography*, **23**, 1, 206-209.

Fisher, A.T., Wheat, G., 2010. Seamounts as conduits for massive fluid, heat and solute fluxes on ridge flanks. *Oceanography*, **23**, 1, 74-87.

Fock, H., Uiblein, F., Köster, F., Von Westernhagen, H., 2002. Biodiversity and species-environment relationships of the demersal fish assemblages at the Great Meteor Seamount (subtropical NE Atlantic), sampled by different trawls. *Mar. Biol.*, **141**, 185–199.

Garcia, M.O., 1996. Turbidites from slope failure on Hawaiian volcanoes. *Geological Society, London, Special Publications*, **110**, 1, 281-294.

Garcia, M.O., & Hull, D.M., 1994. Turbidites from giant Hawaiian landslides: results from Ocean Drilling Program site 842. *Geology*, **22**, 2, 159-162.

Gee, M.J.R., Masson, D.G., Watts, A.B. and Allen, P.A., 1999. The Saharan debris flow: an insight into the mechanics of long runout submarine debris flows. *Sedimentology*, **46**, 317-335.

Giachetti, T., Paris, R., Kelfoun, K., Pérez-Torrado F.J., 2011. Numerical modelling of the tsunami triggered by the Guimar debris avalanche, Tenerife (Canary Islands): comparison with field-based data. *Mar. Geol.*, **284**, 189–202.

Hein, J.R., Conrad, T.A., Staudigel, H., 2010. Seamount mineral deposits: a source of rare metals for high-technology industries, *Oceanography*, **23**, 184–189.

Holland, K.N., Grubbs, R.D., 2007. Fish visitors to seamounts: tunas and billfish at seamounts. *Fish and Aquatic Resources Series*, **12**, 189–201.

Honda, M., Bernatowicz, T., Podosek, F.A., Batiza, R., Taylor, P.T., 1987. Age determinations of eastern Pacific seamounts (Henderson, 6 and 7) - Implications for near-ridgec and intraplate volcanism. *Mar.Geol.*, **74**, 79-84.

Howe, R.W., Sblendorio-Levy, J., 1998. Calcareous nannofossil biostratigraphy and sediment accumulation of turbidite sequences on the Madeira Abyssal Plain, ODP Sites 950–952. *Proc. ODP, Sci. Results*, **157**, 501–515 doi:10.2973/odp.proc.sr.157.129.1998.

Hunt, J.E. 2017. Indentifying and quantifying erosion beneath the deposits of long-runout turbidity currents along their pathway. *Mar. Geolog.*, 389, 32-51.

Hunt, J.E., Jarvis, I., 2017. Prodigious submarine landslides during the inception and early growth of volcanic islands. *Nat. Comms*, 8, 1-12.

Hunt, J.E., Wynn, R.B., Masson, D.G., Talling, P.J., Teagle, D.A.H., 2011. Sedimentological and geochemical evidence for multistage failure of volcanic island landslides: a case study from Icod landslide on north Tenerife. *Geochem*. *Geophys*. *Geosyst.*, **12**, Q12007. doi:10.1029/2011GC003740.

Hunt, J.E., Wynn, R.B., Talling, P.J., Masson, D.G., 2013a. Turbidite record of frequency and source of large volume (>100 km^3) Canary Island landslides in the last 1.5 Ma: implications for landslide triggers and geohazards. *Geochem. Geophys. Geosys.*, **14**, 2100–2123.

Hunt, J.E., Wynn, R.B., Talling, P.J., Masson, D.G., 2013b. Multistage collapse of eight western Canary Island landslides in the last 1.5 Ma: Sedimentological and geochemical evidence from subunits in submarine flow deposits. *Geochem. Geophys. Geosys.*, **14**, 2159–2181.

Hunt, J.E., Wynn, R.B., Talling, P.J., Masson, D.G., 2013c. Frequency and timing of landslide-triggered turbidity currents within the Agadir Basin, offshore NW Africa: Are there associations with climate change, sea-level change and slope sedimentation rates?. *Mar. Geol.*, ***346***, 274-291.

Hunt, J.E., Talling, P.J., Clare, M.A., Jarvis, I., 2014. Long-term (17 Ma) turbidite record of the timing and frequency of large flank collapses of the Canary Islands. *Geochem. Geophys. Geosys.*, **15**, 3322–3345.

Hunt, J.E., Croudace, I.W. and MacLachlan, S.E., 2015a. Use of calibrated ITRAX XRF data in determining turbidite geochemistry and provenance in Agadir Basin, Northwest African passive margin. *Developments in Paleoenvironmental Res*., **17**, 127-146.

Hunt, J.E., Hunt, J.E., Wynn, R.B. and Croudace, I.W., 2015b. Identification, Correlation and Origin of Multistage Landslide Events in Volcaniclastic Turbidites in the Moroccan Turbidite System, *Developments in Paleoenvironmental Res.*, **17**, 147-172 (2015b).

Jarvis I., 2003. in: Jarvis, K.E., Gray, A.L., Houk, R.S. (Eds.), in, *Handbook of Inductively Coupled Plasma Mass Spectrometry*, Viridian Publishing, Woking, UK, 172–224.

Jarvis, I., Moreton, J., Gérard, M., 1998. Chemostratigraphy of Madeira Abyssal Plain Miocene-Pleistocene turbidites, Site 950. *Proc. ODP, Sci. Results*, **157**, 535–558.

Kaschner, K., 2007. Air-breathing visitors to seamounts: marine mammals. Fish and Aquatic Resources Series, **12**, 230–238 (Blackwell, Oxford, 2007).

Koslow, J.A., 1997. Seamounts and the ecology of deep-sea fisheries. *Am. Scientist*, **85**, 168–176.

Lachowycz, S.M., Pyle, D.M., Mather, T.A., Varley, N.R., Odbert, H.M., Cole, P.D. and Reyes-Dávila, G.A., 2013. Long-range correlations identified in time-series of volcano seismicity during dome-forming eruptions using detrended fluctuation analysis. *J. Volcanol. Geotherm. Res.*, **264**, 197–209.

Masson, D.G., Watts, A.B., Gee, M.J.R., Urgeles, R., Mitchell, N.C., Le Bas, T.P. and Canals, M., 2002. Slope failures on the flanks of the western Canary Islands. *Earth Sci. Rev.*, **57**, 1–35.

Miller, K.G., Kominz, M.A., Browning, J.V., Wright, J.D., Mountain, G.S., Katz, M.E., Sugarman, P.J., Cramer, B.S., Christie-Blick, N. and Pekar, S.F., 2005. The Phanerozoic record of global sea-level change. *Science* **310**, 1293–1298.

Milliman, J.D., 1975. Dissolution of aragonite, Mg-calcite, and calcite in the North Atlantic Ocean. *Geology*, **3**, 461–462.

Mitchell, N.C., 2003. Susceptibility of mid-ocean ridge volcanic islands and seamounts to large-scale landsliding. *J. Geophys. Res. Solid Earth*, **108**, B8 1–34.

Mitchell, N.C., Lofi, J., 2008. Submarine and subaerial erosion of volcanic landscapes: comparing Pacific Ocean seamounts with Valencia Seamount, exposed during the Messinian Salinity Crisis. *Basin Research*, **20**, 489-502.

Moore, J.G., Clague, D.A., Holcomb, R.T., Lipman, P.W., Normark, W.R. and Torresan, M.E., 1989. Prodigious submarine landslides on the Hawaiian Ridge. *J. Geophys. Res.*, **94**, 465–17.

Moore, J.G., Normark, W.R., Holcomb R.T., 1994. Giant Hawaiian landslides. *Ann. Rev. Earth Planet. Sci.,* **22**, 119–144.

Morato, T., Kvile, K.Ø., Taranto, G.H., Tempera, F., Narayanaswamy, B.E., Hebbeln, D., Menezes, G.M., Wienberg, C., Santos, R.S. and Pitcher, T.J., 2013. Seamount physiography and biology in the north-east Atlantic and Mediterranean Sea. *Biogeosciences*, **10**, 3039-3054 (2013).

Muhs, D.R., Budahn, J.R., Prospero, J.M., Carey, S.N., 2007. Geochemical evidence for African dust inputs to soils of western Atlantic islands: Barbados, the Bahamas, and Florida. *J. Geophys. Res. Earth Surface*, **112**, F02009 doi:10.1029/2005JF000445.

Murray, J.W., 2014. Ecology and Palaeoecology of Benthic Foraminifera. Routledge, London, 1-389.

Murty, T.S., 2003. Tsunami wave height dependence on landslide volume. *Pure Appl. Geophys.* **160**, 2147–2153.

Omira, R., Ramalho, I., Terrinha, P., Baptista, M.A., Batista, L. and Zitellini, N., 2016. Deep-water seamounts, a potential source of tsunami generated by landslides? The Hirondelle Seamount, NE Atlantic. *Marine Geology*, **379**, 267-280.

Palmiotto, C., Corda, L., Ligi, M., Cipriani, A., Dick, H.J., Douville, E., Gasperini, L., Montagna, P., Thil, F., Borsetti, A.M. and Balestra, B., 2013. Nonvolcanic tectonic islands in ancient and modern oceans. *Geochem. Geophys. Geosys.*, **14**, 4698-4717.

Palmiotto, C., Corda., Bonatti, E., 2017. Oceanic tectonic islands. *Terra Nova*, **29**, 1-12.

Quartau, R., Ramalho, R.S., Madeira, J., Santos, R., Rodrigues, A., Roque, C., Carrara, G. and da Silveira, A.B., 2018. Gravitational, erosional and depositional processes on volcanic ocean islands: Insights from the submarine morphology of Madeira Archipelago. *Earth Planet. Sci. Letts.,* **482**, 288-299.

Pearce, T.J., Jarvis, I., 1992. Composition and provenance of turbidite sands: Late Quaternary: Madeira Abyssal Plain. *Mar. Geol.*, **109**, 21–51.

Pringle, M.S., Staudigel, H., Gee, J., 1991. Jasper Seamount: seven million years of volcanism. *Geology*, **19**, 364-368.

Reynolds, R.L., Belnap, J., Reheis, M., Lamothe, P., Luiszer, F., 2001. Aeolian dust in Colorado Plateau soils: Nutrient inputs and recent change in source. *PNAS*, **98**, 7123–7127.

Reynolds, R.L., Mordecai, J.S., Rosenbaum, J.G., Ketterer, M.E., Walsh, M.K., Moser, K.A., 2010. Compositional changes in sediments of subalpine lakes, Uinta Mountains (Utah): evidence for the effects of human activity on atmospheric dust inputs. *J. Paleolimnol.*, **44**, 161–175.

Rodehorst, U., Schminke, H.-U., Sumita, M., 1998. Geochemistry and petrology of Pleistocene ash layers erupted at Las Canadas Edifice (Tenerife). *Proc. ODP Sci. Results*, **157**, 315–328.

Rogers, A.D., 2004. The biology, ecology and vulnerability of seamount communities. *IUCN*, **12** .

Rothwell, R.G., Alibés, B., Weaver P.P.E., 1998. Seismic facies of the Madeira Abyssal Plain: a correlation between seismic reflection profile and borehole data. *Proc. ODP, Sci. Results*, **157**, 535–558.

Santos, R., Quartau, R., da Silveira, A.B., Ramalho, R., Rodrigues, A. (in press). Gravitational, erosional, sedimentary and volcanic processes on the submarine environment of Selvagen Islands. *Mar Geolog*.

Schmidt, R., Schmincke, H.-U., 2003. Seamounts and Island Building. In (eds Sigurdsson, H., Houghton, B., Mc-Nutt, S., Rymer, H., Stix, J.), Encyclopaedia of Volcanoes, Academic Press, San Diego, California.

Staudigel, H., Koppers, A.A.P., 2015. Seamounts and Island Building. In (eds Siggurdsson, H.) *Encyclopedia of Volcanoes*, 405-421.

Thomson, J., Croudace, I.W., Rothwell, R.G., 2006. A geochemical application of the ITRAX scanner to a sediment core containing eastern Mediterranean sapropel units. *Geological Society, London, Special Publications*, *267*(1), pp.65-77.

Thomson, J., Jarvis, I., Green, D.R.H., Green, D., 1998. Oxidation fronts in Madeira Abyssal Plain turbidites: persistence of early diagenetic trace-element enrichments during burial, Site 950. *Proc. ODP, Sci. Results*, **157**, 559–571.

Totland, M.M., Jarvis, I., Jarvis, K.E., 1992. An assessment of dissolution techniques for the analysis of geological samples by plasma spectrometry. *Chem. Geol.,* **95**, 35–62.

Tucholke, B.E., Smoot, C., 1990. Evidence for age and evolution of Corner seamounts and Great Meteor seamount chain from multibeam bathymetry. *J. Geophys. Res.*, **95**, B11, 17555–17569.

Van den Bogaard, P., 2013. The origin of the Canary Island Seamount Province – New ages of old seamounts. *Scientific Reports*, **3**, 2107.

Vogt, P.R., Smoot, N.C., 1984. The Geisha Guyots: multi- beam bathymetry and morphometric interpretation. *J. Geo- phys. Res.*, **89**, 11085-11107.

Weaver, P.P.E., 2003. Northwest Africa continental margin: history of sediment accumulation, landslide deposits, and hiatuses as revealed by drilling the Madeira Abyssal Plain. *Paleoceanography*, **18**, 1–12.

Weaver, P.P.E., Kuijpers, A., 1983. Climatic control on turbidite deposition on the Madeira Abyssal Plain, *Nature*, **306**, 360-363.

Weaver, P.P.E., Jarvis, I., Lebreiro, S.M., Alibes, B., Baraza, J., Howe, R. and Rothwell, R.G., 1998. The Neogene turbidite sequence on the Madeira Abyssal Plain – a history of basin filling and early diagenesis. *Proc. ODP Sci. Results*, **157**, 619–634.

Weaver, P.P.E., Rothwell, R.G., Ebbing, J., Gunn, D. and Hunter, P.M., 1992. Correlation, frequency of emplacement and source directions of megaturbidites on the Madeira Abyssal Plain. *Mar. Geol.*, **109**, 1–20.

Wendt, I., Kreuzer, H., Müller, P., von Rad, U., Raschka, H., 1976. K-Ar age of basalts from Great Meteor and Josephine seamounts (eastern North Atlantic). *Deep Sea Res. Abs*., **23**, 849–862.

Wessel, P., Sandwell, D.T., Kim, S.-S., 2010. The Global Seamount Census. *Oceanography*, **23**, 1, 24-33.

Wynn, R.B., Weaver, P.P.E., Masson, D.G., Stow D.A.V., 2002. Turbidite depositional architecture across three interconnected deep-water basins on the northwest African margin. *Sedimentology*, **49**, 1441–1462 doi:10.1046/j.1365-3091.2002.00471.x.

Yesson, C., Clark, M.R., Taylor, M.L., Rogers, A.D., 2011. The global distribution of seamounts based on 30 arc seconds bathymetry data. *Deep Sea Res. Part 1*, **58**, 442–453.

Figures and Captions

Figure 1 | Map of the Madeira Abyssal Plain featuring the provenances and pathways of turbidites recorded at ODP Sites 950, 951 and 952. Shown are the major seamounts that comprise the Great Meteor-Cruiser complex and pathways (in white) to the ODP Sites. Also shown are provenance pathways for the grey volcaniclastic and pale-grey 'non-volcaniclastic' turbidites from the Canary Islands (red) and from the different continental slope provenances: offshore NW Morocco (intermediate green), offshore Western Sahara (pale green) and offshore Mauritania (dark green). The outline of Madeira Abyssal Plain at 5,300 m water depth is given by the yellow line.

Figure 2 | Examples of the different beds associated with flank collapse and volcanism of the Great Meteor-Cruiser seamount complex. Panels show core photographs, facies identification and expanded magnified inlays adapted from Schminke *et al.* (1995). Inlays (a) two fining-upwards units in the base of a white calciclastic turbidite; (b) coarse-grained carbonate debris and coarse 2–5 cm clasts of basalt; and (c) ripple-laminations of medium-grained volcaniclastic (basaltic) sandstone.

Figure 3 | Geochemical cross plots of the turbidite mudcap compositions from Canary Island and seamount-sourced submarine landslides from ODP Site 950. Clusters within groups of white and brown calciclastic turbidites may indicate different Great Meteor or Cruiser seamount sources. Trends within a) show variations in Sr, although offsets away from the general trend may reflect variable diagenesis; b) scatter of TiO_2 likely reflects variations in volcaniclastic content; c) Fe_2O_3 and Zr scatter may reflect variations in volcaniclastic and Saharan dust content; and d) MgO and K_2O scatter may reflect variations in shallow-water carbonate content (incorporation of Mg-calcite) and detrital volcaniclastics. CFB = carbonate-free basis.

Figure 4 | Simplified model of the lifecycle of the Great Meteor-Cruiser seamount complex. Model shows timing of inception, rapid vertical ascension, emergence, prodigious flank collapse, rejuvenation of volcanism, cessation of volcanism, and thermal subsidence of dormant edifice against the timing of calciclastic turbidites, coarse-grained black volcaniclastic turbidites and tephras.

Figure 5 | Temporal record of post-17 Ma turbidites from ODP sites on the Madeira Abyssal Plain. Compositional changes in the white calciclastic and brown calciclastic turbidites are shown. Major-element oxides and trace elements (excluding Sr) shown on a carbonate-free basis (CFB). Volcanic history of seamounts taken from Tucholke and Smoot (1990) with solid bars representing ages of volcanism supported by absolute age-dating and dashed-lines representing inferred ages of activity. Horizontal yellow and brown bars represent temporal clusters of white-calciclastic turbidites and brown-calciclastic turbidites, respectively.

Figure 6 | Comparison of the timing of white (yellow boxes) and brown (brown boxes) calciclastic turbidites since 7.0 Ma at ODP Site 950 with the relative sea-level curve of Miller *et al*. (2005). In addition, log–log plots of the probability of exceedance of the timing between turbidite events over the last 43 Myr show near perfect log–log distributions albeit for coarse-tails (largest recurrence intervals) to the dataset.

Figure 7 | White calciclastic turbidite beds >10 cm-thickness showing presence or lack of sub-units (multiple fining-upwards units). Sub-units highlighted by arrows. Oxidation fronts (cf. Thomson *et al.* 1998) highlighted by 'ox'. Greyscale profiles overlain on the core photographs to interrogate the visual identification of sub-units. Bed designation and age given below the bed, based on Hunt *et al.* (2014).

Supplementary Materials

Supplement 1 | Core panel of ODP Core 950A in the Madeira Abyssal Plain present to 4.79 Ma.
Core panel shows each section with core photograph, turbidite type and letter designations based on lithostratigraphic and geochemical criteria (Weaver *et al.* 1992; Jarvis *et al.* 1998; Hunt *et al.* 2014; Hunt & Jarvis, 2017), and biostratigraphic ages (Howe & Sblendorio-Levy, 1998). Core panel extends from the present-day seafloor (0 m metres below seafloor, mbsf, top left) to 160 mbsf (bottom right), dated at 4.79 Ma. Headers are core numbers and depths of core tops.

Supplement 2 | Core panel of ODP Core 950A in the Madeira Abyssal Plain 4.79 to 18.1 Ma.
Core panel shows each section with core photograph, turbidite type and letter designations based on lithostratigraphic and geochemical criteria (Weaver *et al.* 1992; Jarvis *et al.* 1998; Hunt *et al.* 2014; Hunt & Jarvis, 2017), and biostratigraphic ages (Howe & Sblendorio-Levy, 1998). Core panel extends from 160 mbsf (4.79 Ma, top left) to 333 m at 18.1 Ma (bottom right). Headers are core numbers and depths of core tops.

Supplement 3 | Core panel of ODP Core 950A in the Madeira Abyssal Plain 18 to 43 Ma.
Core panel shows each section with core photograph and turbidite designations based on lithostratigraphic and geochemical criteria (Weaver *et al.* 1992; Jarvis *et al.* 1998; Hunt *et al.* 2014; Hunt & Jarvis, 2017), and biostratigraphic ages (Howe & Sblendorio-Levy, 1998). Core panel extends from 333 mbsf (18.1 Ma, top left) to 372 m at 43 Ma (bottom right). Headers are core numbers and depths of core tops. Tephra horizons are indicated by arrows with 'T' symbols. Dates of the proposed inception for the seamounts of the Great Meteor-Cruiser seamount complex (Tucholke and Smoot, 1990) are plotted vs. turbidite age, type and thickness.

Supplement 4 | Hemipelagite depth against time for ODP Sites 950 (black), 951 (orange) and 952 (blue) showing hemipelagites depths of coccolith first and last occurrences with error bars (circles) (Hunt *et al*. 2014; Hunt and Jarvis, 2017).
Lithostratigraphy of the hemipelagite records periods of sea-level change, manifested in the Marine Isotope Stage record, whereby: (1) at high sea-level there is greater calcium carbonate preservation forming white calcareous oozes younger than 2.5 Ma or pale brown to light grey hemipelagites in the older record; (2) and dark brown clays are deposited during lowstands younger than 2.5 Ma and dark grey clays in the older record. Also shown are the biostratigraphic age controls up to 15 Ma for each ODP Site.

Supplement 5 | Detailed methodology for turbidite volume calculations.

Supplement 6 | Seismic stratigraphy of the Madeira Abyssal Plain tied to ODP Core 950[7]. Data shows the simple layer-cake stratigraphy present that is used to generate single bed volumetrics based upon decompaction of single beds with seismic packages (Rothwell *et al*. 1998; Hunt *et al*. 2014; Hunt and Jarvis, 2017).

Supplement 7 | Isopach maps of Beds B, D, E, F and G in the Madeira Abyssal Plain based upon piston core coverage of the deposits. Data shows the thickness variations and limits of the deposits across the depocentres that can be use to constrain the deposit volumes.

Supplement 8 | Table of turbidite volumes of beds in the Madeira Abyssal Plain for deposits over the last 700 kyrs. Data shows complementary data used to report the volumes of these beds and how they compare to the volume estimates of the current study.

Supplement 9 | Table of turbidite volumes of calciclastic beds in the Madeira Abyssal Plain for deposits over the last 17 Myrs. Data shows the thicknesses of deposits at each ODP site and their conversion to decompacted volumes.

Acknowledgements

IJ acknowledges support from NERC ODP grant GST/02/1097. JH acknowledges support from NERC grant NE/T002034/1 where these seamounts represent a contrast to the rapidly grown volcanic edifice surveyed during the project.

JH and IJ would like to thank the input of the reviewers and editor during preparation of this manuscript that has made the work more thorough and impactful.

Figure 1

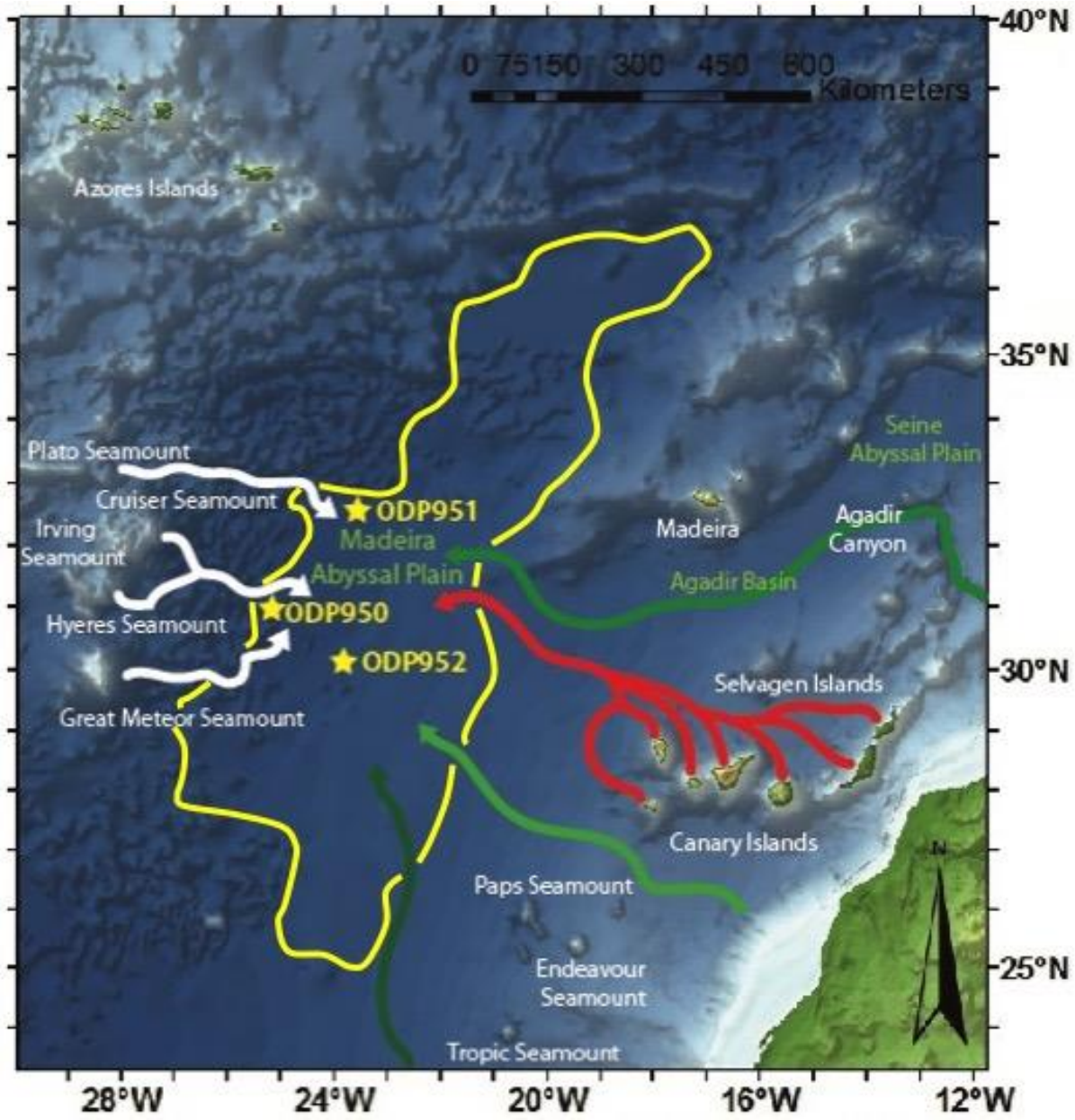

Figure 1 | Map of the Madeira Abyssal Plain featuring the provenances and pathways of turbidites recorded at ODP Sites 950, 951 and 952. Shown are the major seamounts that comprise the Great Meteor-Cruiser complex and pathways (in white) to the ODP Sites. Also shown are provenance pathways for the grey volcaniclastic and pale-grey 'non-volcaniclastic' turbidites from the Canary Islands (red) and from the different continental slope provenances: offshore NW Morocco (intermediate green), offshore Western Sahara (pale green) and offshore Mauritania (dark green). The outline of Madeira Abyssal Plain at 5,300 m water depth is given by the yellow line.

Figure 2

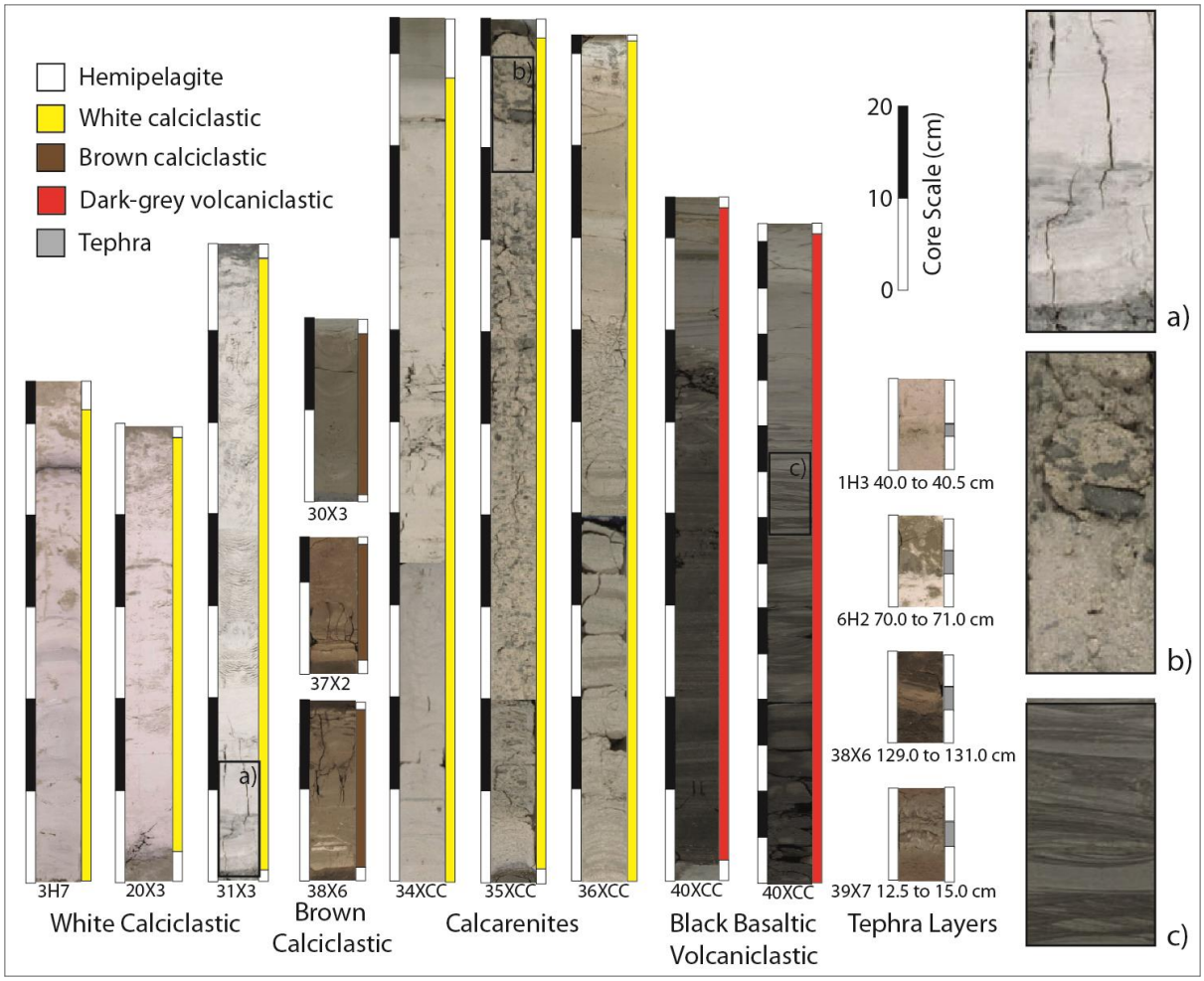

Figure 2 | Examples of the different beds associated with flank collapse and volcanism of the Great Meteor-Cruiser seamount complex. Panels show core photographs, facies identification and expanded magnified inlays adapted from Schminke *et al.* (1995). Inlays (a) two fining-upwards units in the base of a white calciclastic turbidite; (b) coarse-grained carbonate debris and coarse 2–5 cm clasts of basalt; and (c) ripple-laminations of medium-grained volcaniclastic (basaltic) sandstone.

Figure 3

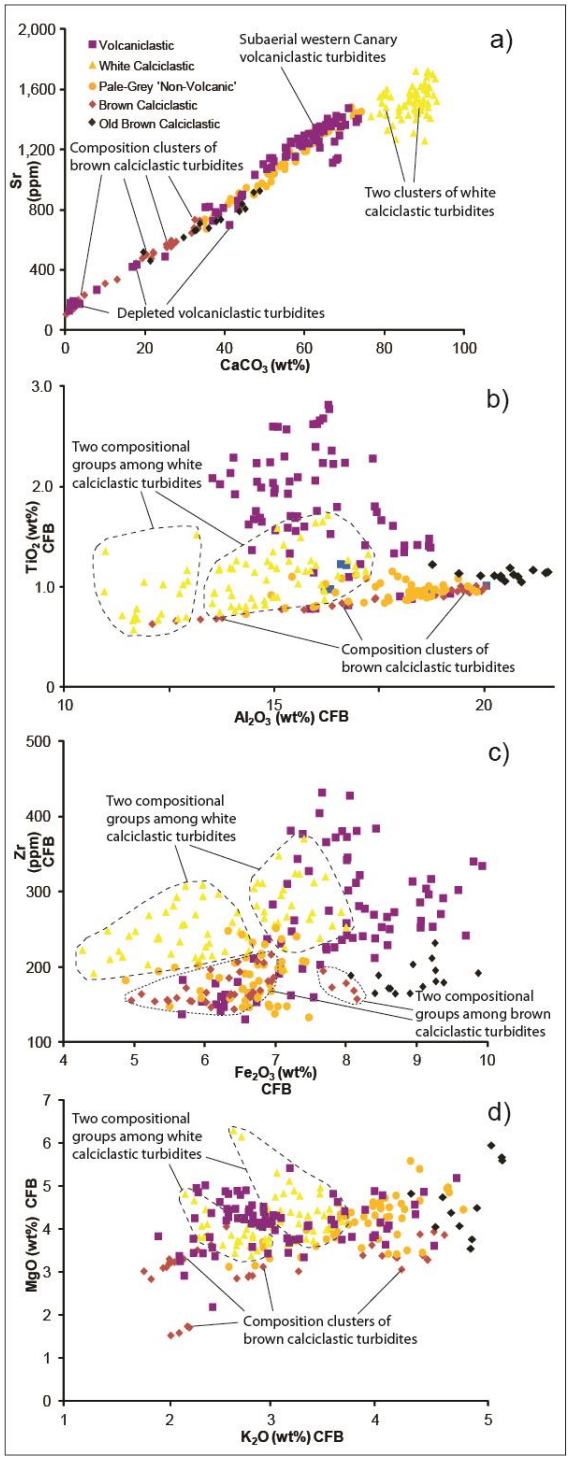

Figure 3 | Geochemical cross plots of the turbidite mudcap compositions from Canary Island and seamount-sourced submarine landslides from ODP Site 950. Clusters within groups of white and brown calciclastic turbidites may indicate different Great Meteor or Cruiser seamount sources. Trends within a) show variations in Sr, although offsets away from the general trend may reflect variable diagenesis; b) scatter of TiO_2 likely reflects variations in volcaniclastic content; c) Fe_2O_3 and Zr scatter may reflect variations in volcaniclastic and Saharan dust content; and d) MgO and K_2O scatter may reflect variations in shallow-water carbonate content (incorporation of Mg-calcite) and detrital volcaniclastics. CFB = carbonate-free basis

Figure 4

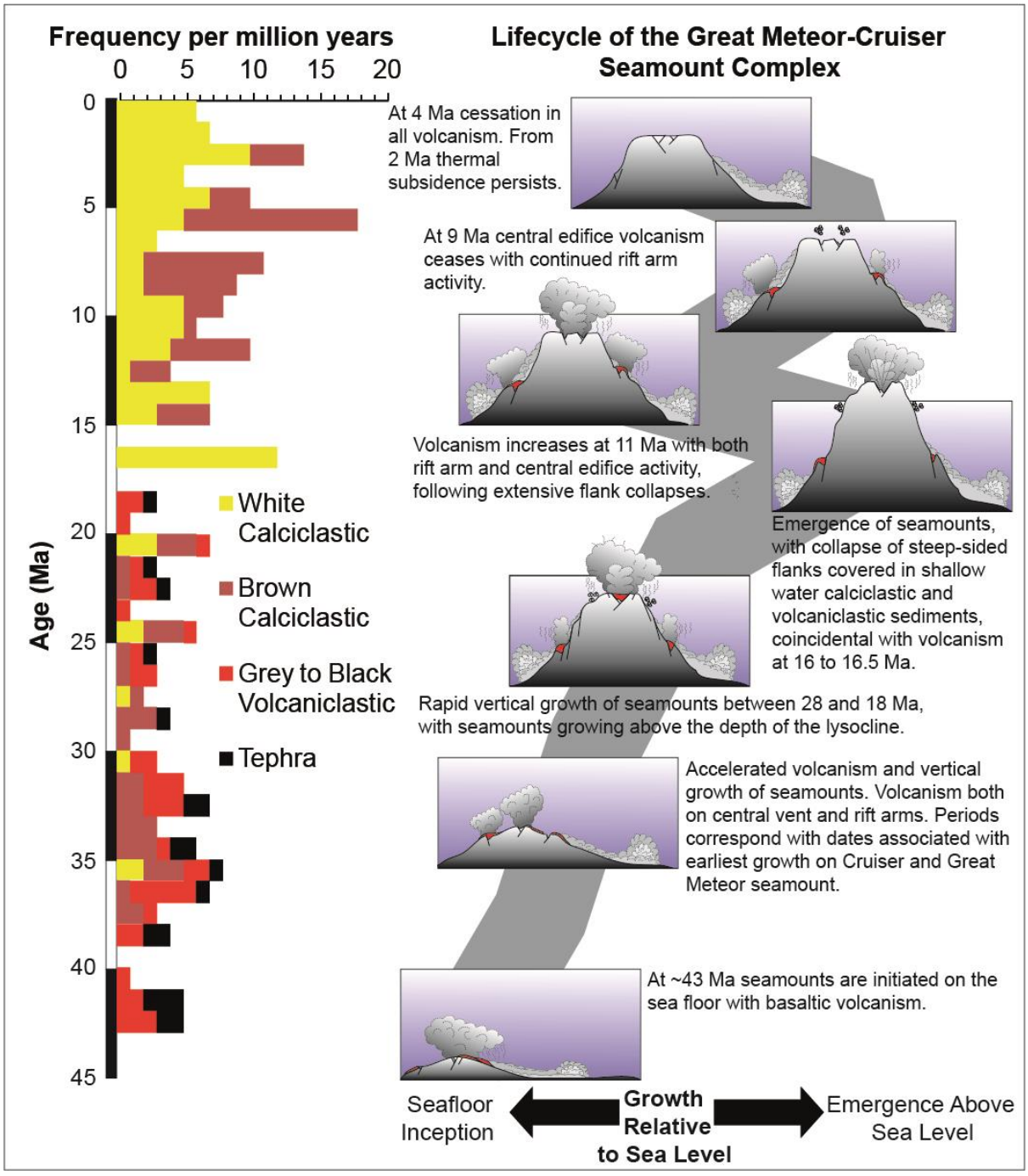

Figure 4 | Simplified model of the lifecycle of the Great Meteor-Cruiser seamount complex. Model shows timing of inception, rapid vertical ascension, emergence, prodigious flank collapse, rejuvenation of volcanism, cessation of volcanism, and thermal subsidence of dormant edifice against the timing of calciclastic turbidites, coarse-grained black volcaniclastic turbidites and tephras.

Figure 5

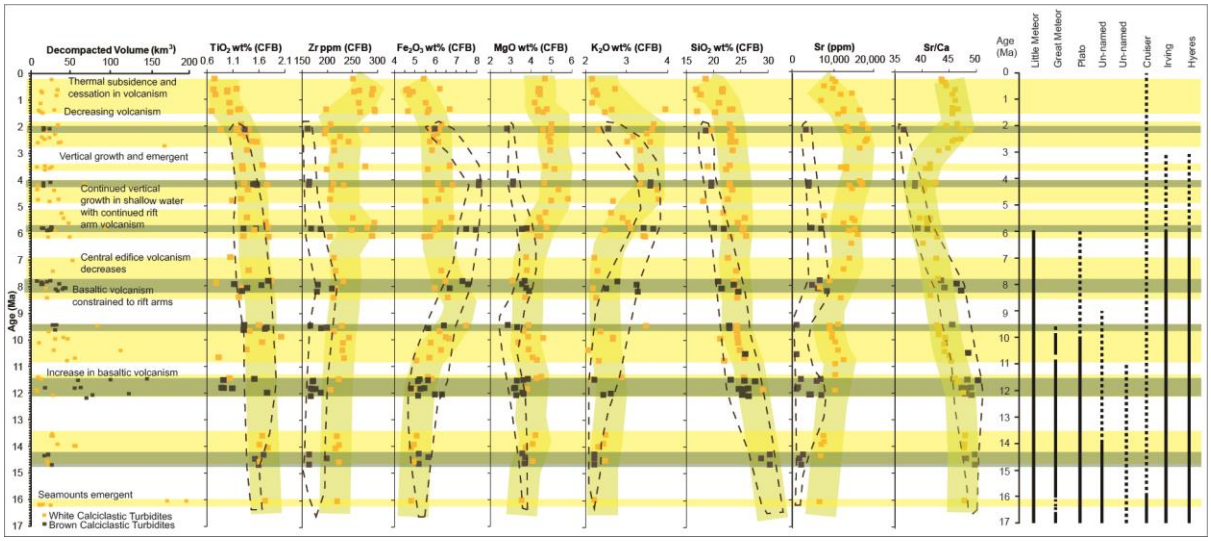

Figure 5 | Temporal record of post-17 Ma turbidites from ODP sites on the Madeira Abyssal Plain. Compositional changes in the white calciclastic and brown calciclastic turbidites are shown. Major-element oxides and trace elements (excluding Sr) shown on a carbonate-free basis (CFB). Volcanic history of seamounts taken from Tucholke and Smoot (1990) with solid bars representing ages of volcanism supported by absolute age-dating and dashed-lines representing inferred ages of activity. Horizontal yellow and brown bars represent temporal clusters of white-calciclastic turbidites and brown-calciclastic turbidites, respectively.

Figure 6

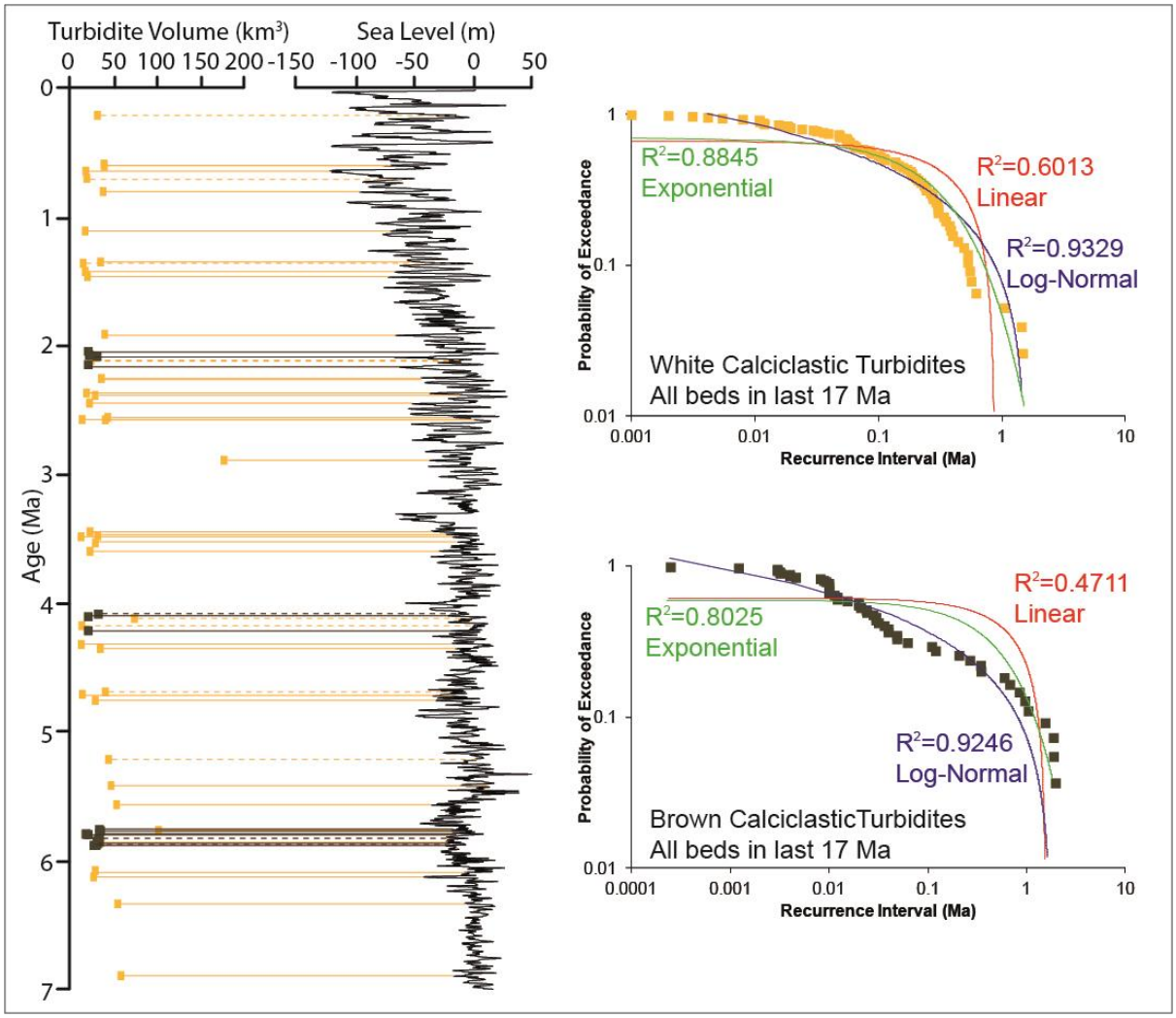

Figure 6 | Comparison of the timing of white (yellow boxes) and brown (brown boxes) calciclastic turbidites since 7.0 Ma at ODP Site 950 with the relative sea-level curve of Miller *et al*. (2005). In addition, log–log plots of the probability of exceedance of the timing between turbidite events over the last 43 Myr show near perfect log–log distributions albeit for coarse-tails (largest recurrence intervals) to the dataset.

Figure 7

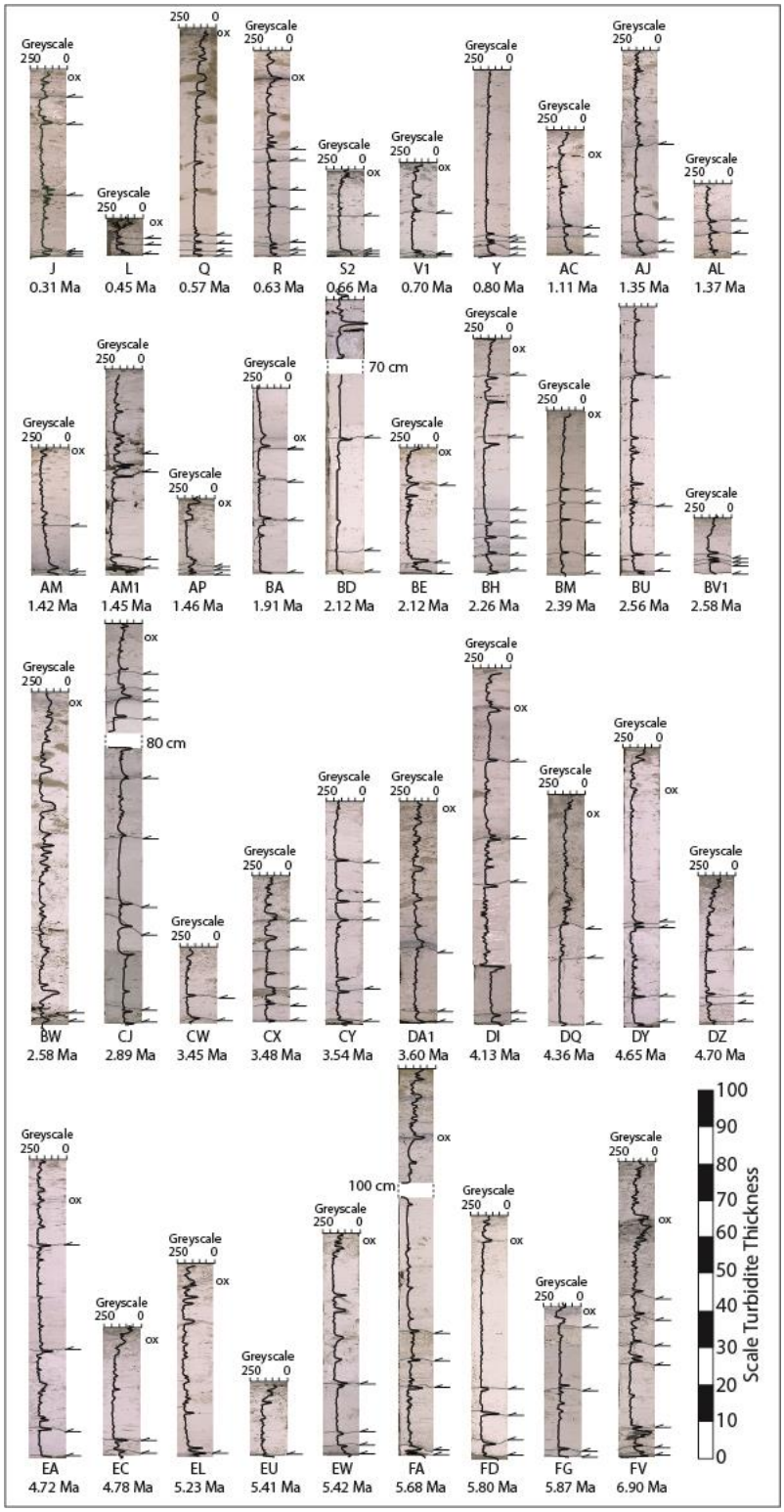

Figure 7 | White calciclastic turbidite beds >10 cm-thickness showing presence or lack of sub-units (multiple fining-upwards units). Sub-units highlighted by arrows. Oxidation fronts (cf. Thomson *et al.* 1998) highlighted by 'ox'. Greyscale profiles overlain on the core photographs to interrogate the visual identification of sub-units. Bed designation and age given below the bed, based on Hunt *et al.* (2014).

Table 1. Diagnostic criteria for different sediment types.

Sediment	**Subdivision**	**Origin**	**Colour**	**Bioturbation**	**Magnetic Suscept.**	**$CaCO_3$**	**Sr**	**TiO_2 (CFB)**	**Fe_2O_3 (CFB)**	**Al_2O_3 (CFB)**
Hemipelagite	Dispersed foraminifera and abundant coccoliths, fined-grained, reduced organic carbon content, higher calcium carbonate content, and moderate-to-high bioturbation.									
	White interglacial	Background sediment.	White	High	Low	> 56 wt%	> 1200 ppm	Negligible	N/A	
	Brown glacial		Red-brown	Moderate	Low-Med	0.5-35 wt%	< 1200 ppm	< 0.5 wt%	N/A	
	Pre-7.5 Myr hemipelagite		Grey-brown	Low	Low-Med	N/A				
Seamount Turbidite	Fine-grained, decimetre-to-metre-thick mudcaps above basal upwards-fining, fine-sands and silts. Distinct, sharp basal contact.									
	White calciclastic	Failure of seamount cover above the CCD.	White	None	None	> 78 wt%	> 1200 ppm	Negligible	0.45-1.45 wt%	1.4-3.8 wt%
	Brown calciclastic	Failure of seamount cover below CCD.	Red-brown	None	Low-Med	0.5-42 wt%	< 1450 ppm	< 1 wt%	4.0-6.8 wt%	9.8-17.3 wt%
	Black volcaniclastic	Failure of seamount volcaniclastic sediment.	Black-dark grey	None	High	N/A Note negligible carbonate content.				

CFB = carbonate-free basis

Table 2. Diagnostic criteria for different sediment types.

Criteria	Rationale	Implications
Sr and Sr/Ca	Strontium and Sr/Ca values of pelagic sediments have been used as a proxy for aragonite content (Thomson et al. 2006), which is produced and preserved preferentially in shallow-water environments. Thus, low Sr and Sr/Ca ratios imply low aragonite content and a deeper water provenance	White calciclastic turbidites likely represent failures of carbonate-rich pelagite draping se`mounts above the carbonate-compensation depth (CCD), and probably above the aragonite lysocline, (Jarvis et al. 1998). We suggest that these beds will likely have diagnostically higher Sr and Sr/Ca. In contrast, we suggest that the low carbonate and low Sr contents of the brown calciclastic turbidites indicate that they were probably sourced from failure of carbonate-poor, aragonite-depleted, sediments deposited at greater water depths below the aragonite-compensation depth (ACD; 2–3 km, in the modern North Atlantic; e.g. Milliman, 1975), and perhaps below the calcite lysocline at 4.05–4.35 km, but above the CCD at >4.65 km (Milliman, 1975; Berger, 1978; Baslam, 1983).
K and Mg	Although K has been used as a proxy for clay content it can also provide insight into the volcanic provenance of sediments or how potassic a particular volcanic system was (Croudace et al. 2006; Hunt et al., 2014, 2015a, 2015b; Hunt & Jarvis, 2017).	Here, we compare K and Mg that may discriminate different volcanic sources. Increasing K is interpreted as indicative of the changing volcanism beneath the seamounts. Differences in these elements, in a carbonate-free-basis have previously discriminated the provenance of these beds from Madeira or Canary Island sources (Hunt et al. 2014; Hunt & Jarvis, 2017).
Ti and Al	Ti is used as an indicator of volcanic heavy minerals, while Al is used as an indicator of detrital clays (Croudace et al. 2006; Hunt et al., 2015a, 2015b).	Here, we compare Ti and Al to reduce the relative input of volcanic materials to sediments that have likely been chemically weathered.
Fe and Zr	Increased Fe content has been associated with increased volcanic content, specifically of basic composition (Hunt et al. 2014, 2015a, 2015b; Hunt & Jarvis 2017). Zr in North Atlantic sediments may be linked to presence of coarse zircons from a Saharan dust source (Castillo et al. 2008).	Here, we compare Zr and Fe to discriminate the relative importance of volcanic or Saharan dust input, such that periods of reduced volcanism and increased exposure to sediments settled from Saharan dust storms.

Supplement 1

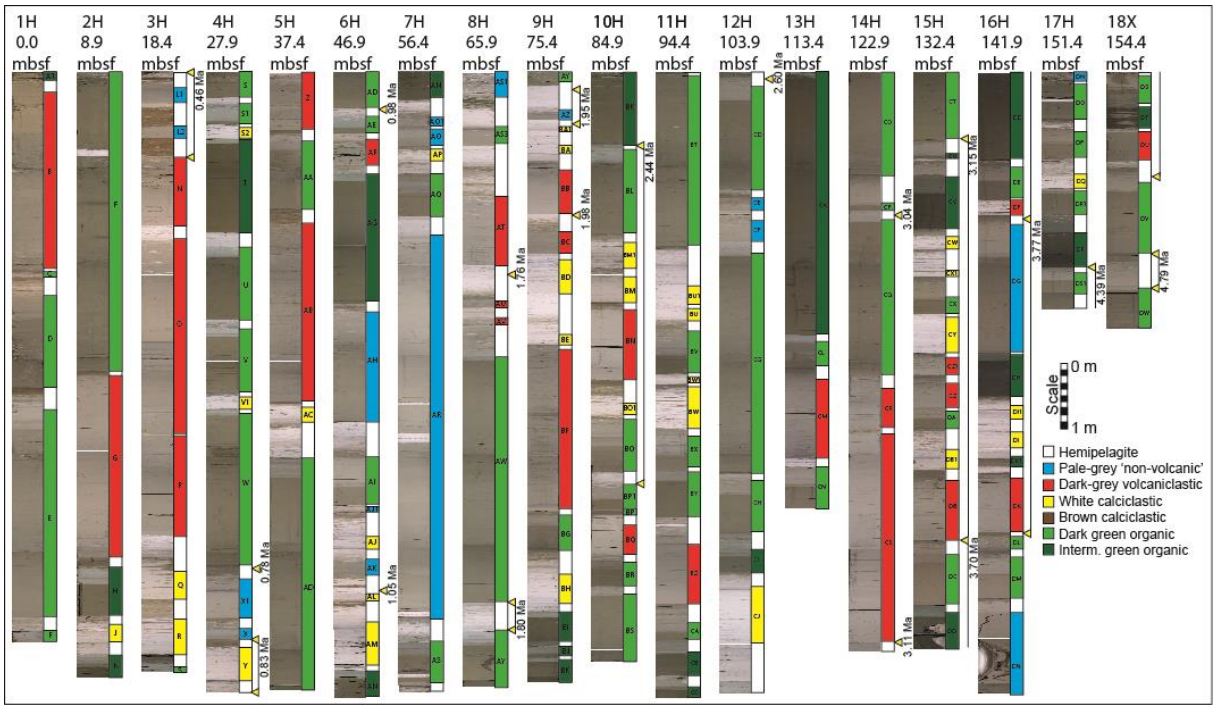

Supplement 1 | Core panel of ODP Core 950A in the Madeira Abyssal Plain present to 4.79 Ma.

Core panel shows each section with core photograph, turbidite type and letter designations based on lithostratigraphic and geochemical criteria (Weaver *et al.* 1992; Jarvis *et al.* 1998; Hunt *et al.* 2014; Hunt & Jarvis, 2017), and biostratigraphic ages (Howe & Sblendorio-Levy, 1998). Core panel extends from the present-day seafloor (0 m metres below seafloor, mbsf, top left) to 160 mbsf (bottom right), dated at 4.79 Ma. Headers are core numbers and depths of core tops.

Supplement 2

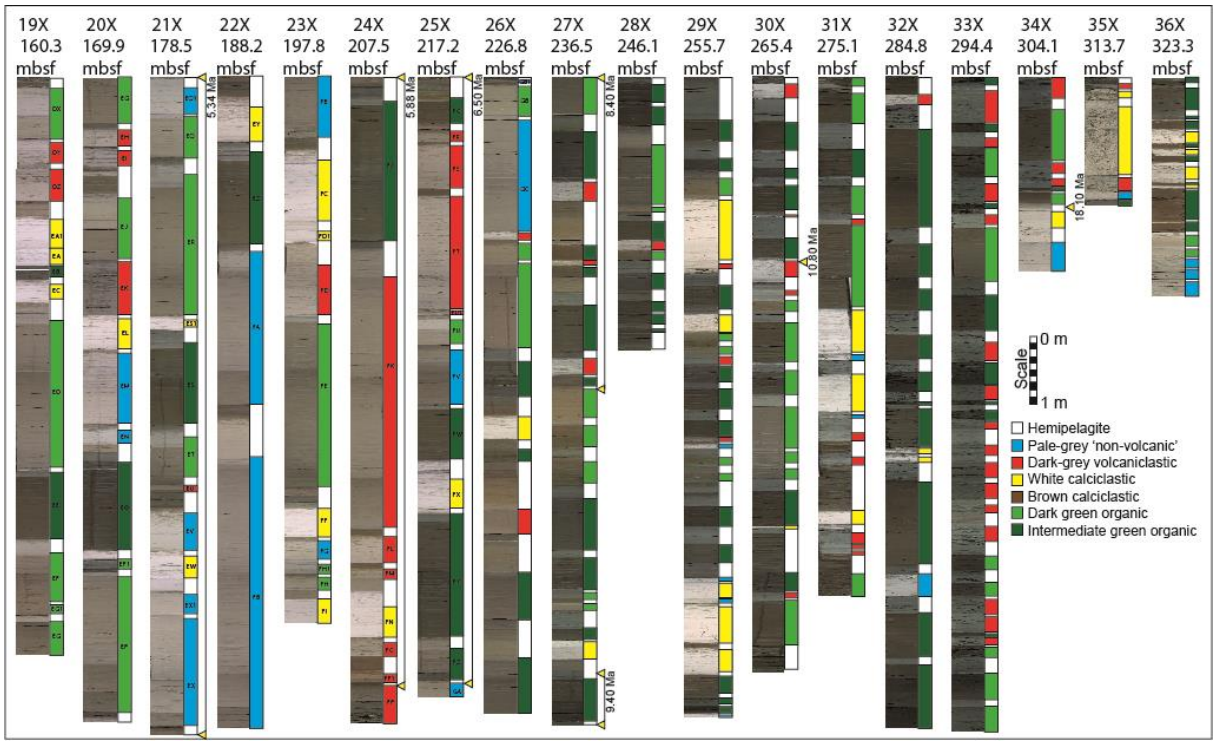

Supplement 2 | Core panel of ODP Core 950A in the Madeira Abyssal Plain 4.79 to 18.1 Ma.
Core panel shows each section with core photograph, turbidite type and letter designations based on lithostratigraphic and geochemical criteria (Weaver *et al.* 1992; Jarvis *et al.* 1998; Hunt *et al.* 2014; Hunt & Jarvis, 2017), and biostratigraphic ages (Howe & Sblendorio-Levy, 1998). Core panel extends from 160 mbsf (4.79 Ma, top left) to 333 m at 18.1 Ma (bottom right). Headers are core numbers and depths of core tops.

Supplement 3

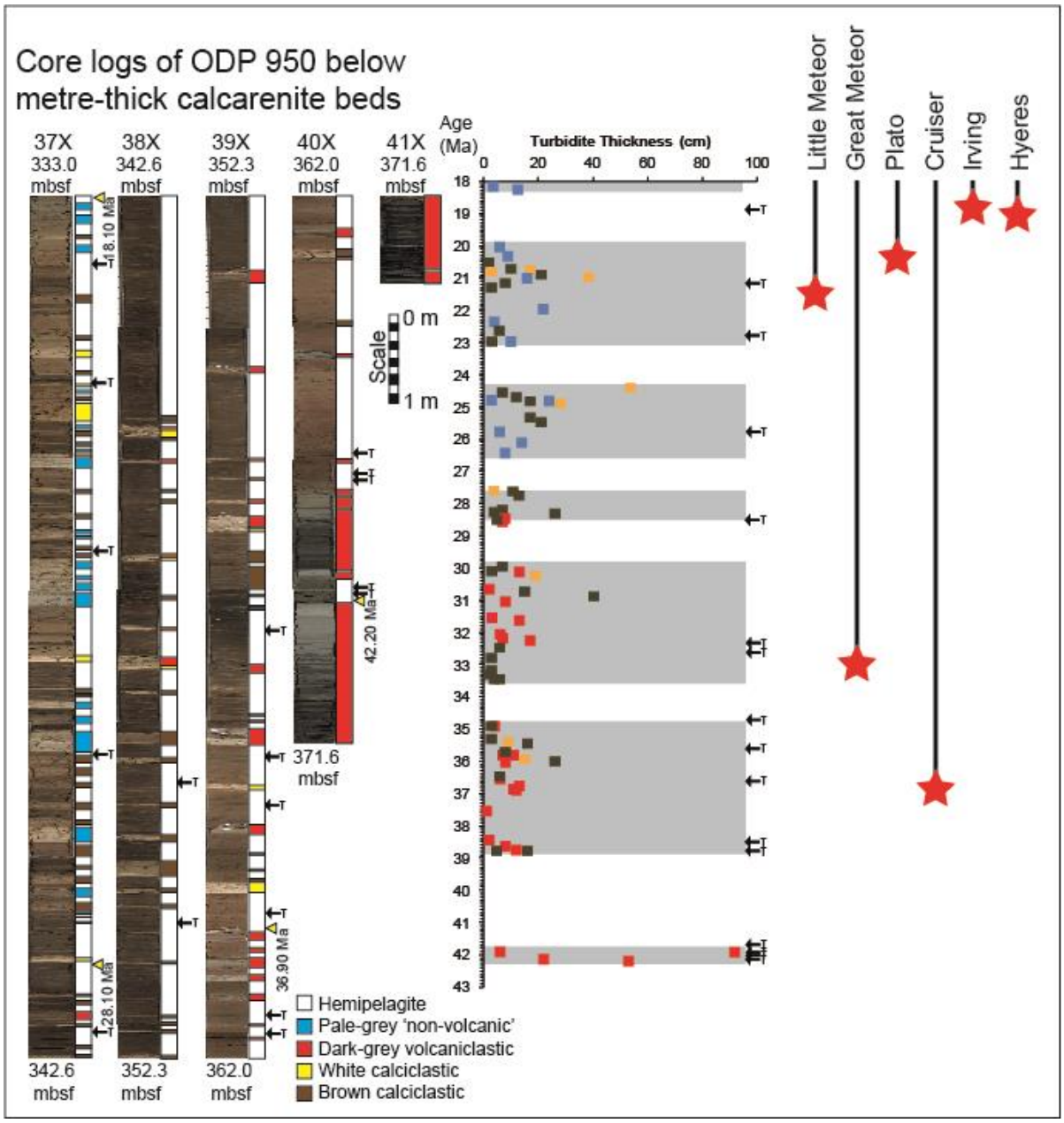

Supplement 3 | Core panel of ODP Core 950A in the Madeira Abyssal Plain 18 to 43 Ma. Core panel shows each section with core photograph and turbidite designations based on lithostratigraphic and geochemical criteria (Weaver *et al.* 1992; Jarvis *et al.* 1998; Hunt *et al.* 2014; Hunt & Jarvis, 2017), and biostratigraphic ages (Howe & Sblendorio-Levy, 1998). Core panel extends from 333 mbsf (18.1 Ma, top left) to 372 m at 43 Ma (bottom right). Headers are core numbers and depths of core tops. Tephra horizons are indicated by arrows with 'T' symbols. Dates of the proposed inception for the seamounts of the Great Meteor-Cruiser seamount complex (Tucholke and Smoot, 1990) are plotted vs. turbidite age, type and thickness.

Supplement 4

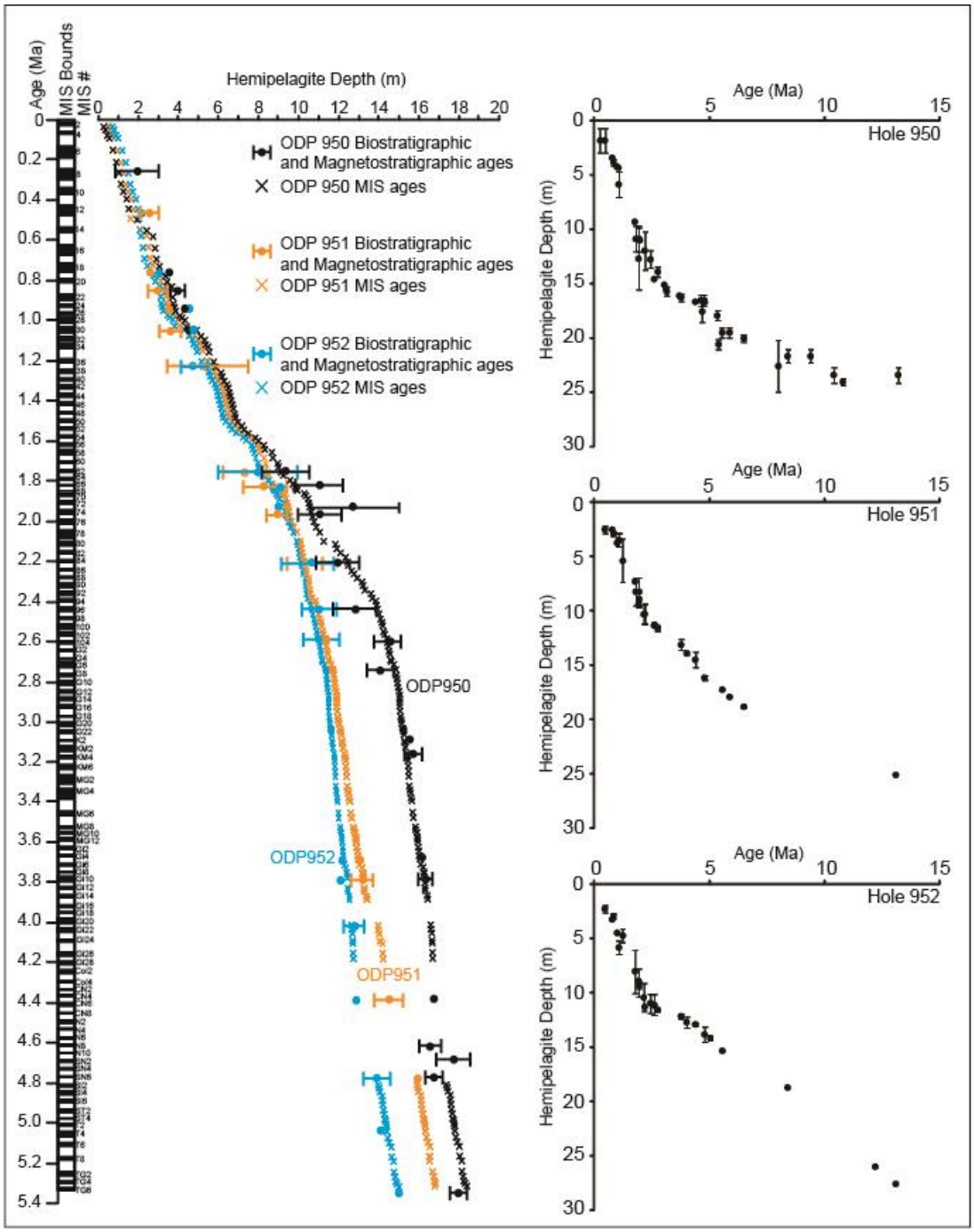

Supplement 4 | Hemipelagite depth against time for ODP Sites 950 (black), 951 (orange) and 952 (blue) showing hemipelagites depths of coccolith first and last occurrences with error bars (circles) (Hunt *et al*. 2014; Hunt and Jarvis, 2017). Lithostratigraphy of the hemipelagite records periods of sea-level change, manifested in the Marine Isotope Stage record, whereby: (1) at high sea-level there is greater calcium carbonate preservation forming white calcareous oozes younger than 2.5 Ma or pale brown to light grey hemipelagites in the older record; (2) and dark brown clays are deposited during lowstands younger than 2.5 Ma and dark grey clays in the older record. Also shown are the biostratigraphic age controls up to 15 Ma for each ODP Site.

Supplement 5 | Detailed methodology for turbidite volume calculations.

The magnitude of submarine landslides from the Great Meteor Seamount Complex is inferred from the calculated volumes of the associated turbidites. Due to the burial depth of the older strata in the Madeira Abyssal Plain, the calculated volumes require decompaction to enable valid comparison between multiple depths (Hunt et al. 2014; Hunt & Jarvis, 2017). These decompacted volumes better represent the volume of the turbidite at the point of deposition. However, a caveat is that the turbidite volume may not represent the accurate measure of the landslide volume as: 1) not all the landslide may have disaggregated into a turbidity current; and 2) the turbidity current may have increased in volume by 10-50% due to erosion of the seafloor beneath the turbidity current on the seamount slope and across the Madeira Abyssal Plain (Hunt, 2017). However, turbidite volume does give an representation of the scale of the original landslide, and dowa represent close approximations of the landslide volume (Hunt et al. 2014; Hunt & Jarvis, 2017).

The stratigraphy at ODP Sites 950-952 have previously been tied to a dense network of 2D seismic reflection lines via an established seismic stratigraphy linking a number of key seismic reflectors to distinctive sedimentary horizons (e.g. Supplement 6) (Alibes et al. 1996, 1999; Rothwell et al. 1998; Hunt et al. 2014; Hunt & Jarvis, 2017). These delineated seismic packages have previously been correlated across the Madeira Abyssal Plain and linked to sediment packages of 10s-to-100s metres of turbidite beds and hemipelagite in the ODP Cores. Isopachs of these seismic packages have previously provided *in-situ* volumes (Alibes et al. 1996, 1999; Rothwell et al. 1998), and have also been decompacted to give decompacted volumes for those sediment packages across the basin.

Turbidite thicknesses are taken from ODP Cores (950-952), and the sediment columns have been decompacted to provide decompacted thicknesses for each turbidite. The decompacted thicknesses of each buried turbidite in the Madeira Abyssal Plain have previously been calculated (Hunt et al. 2014; Hunt & Jarvis, 2017). The decompacted thickness of each turbidite is compared to the decompacted thicknesses of the entire seismic package in which it is. The proportion of the overall decompacted seismic package thickness represented by each decompacted turbidite is multiplied by the established decompacted volume of the seismic package to provide the decompacted volume of each turbidite (Alibes et al. 1996, 1999; Rothwell et al. 1998; Hunt et al. 2014; Hunt & Jarvis, 2017). This is completed for each bed and repeated at each ODP Site to understand the uncertainty in the volumes calculated, which is generally between 10 and 25% (17±9%) for the calciclastic turbidites in the last 7 Myr (e.g. Supplement 9), for beds older than 7 Myr this is based upon thickness at ODP Site 950 that best recovers this period.

A second method for calculating decompacted turbidite thickness from combining data from ODP cores and correlated seismic reflection profiles over the Madeira Abyssal Plain was completed based upon Alibes et al. (1996, 1999). The decompacted turbidite thicknesses from this study based upon Hunt et al. (2014) and Hunt and Jarvis (2017) showed a variation of 15±8% from those calculated using the Alibes et al. (1996, 1999) method.

It is important to compare the above method of calculating turbidite volumes by comparing to existing data and complementary methods of calculating turbidite volumes. Previous studies have calculated the volumes of all the most recent turbidites (last 700 kyr from all sources) in the Madeira Abyssal Plain recovered in about 300 piston cores across the system (Weaver et

al. 1992; Rothwell et al. 1992; Hunt et al. 2013c; Hunt, 2017). Comparison of these published turbidite volumes to those proposed here, shows a strong correlation (R^2 = 0.95) but were generally, and consistently, 33% larger than previous estimates (e.g. Supplement 8). Secondly, the average decompacted turbidite volumes from the ODP sites (using the above method) were compared to volumes calculated from taking the average turbidite thickness (decompacted) from the same ODP cores and simply multiplying across the 65,000 km^2 area of the Madeira Abyssal Plain to the -5,200 m contour (e.g. Supplement 7). These results correlated very well (R^2 = 0.98), but showed that taking a simple average turbidite thickness and multiplying across the basin area produced volumes 33% larger than those based upon a proportion of an established basin sediment volume constrained by seismic reflection surveys (e.g. Supplement 8).

In addition, here, turbidite volumes for the last 700 kyr turbidites have also been calculated from 1) average thickness projected across the larger area of the open basin at the -5,000 m contour (80,000 km^2); and 2) iospach maps generated from use of all bed thicknesses recovered from a dataset of about 300 piston cores (e.g. Supplement 7). Here, the turbidite volumes from average turbidite thicknesses in piston cores correlated to those calculated using the above method decompaction method (R^2 = 0.90); but were generally 40% larger, but this could be accounted for by decompaction, as the piston core volumes were not decompacted (e.g. Supplement 8). Isopachs of turbidites based on the piston core coverage were also not decompacted, but did account for greater potential spatial thickness variability. These turbidite isopachs correlated with the calculated decompacted volumes based upon the ODP core decompacted thicknesses (R^2 = 0.93), with only a 5% difference.

We are therefore confident that the method of estimating turbidite volumes from the decompacted turbidite thicknesses from the ODP cores is robust.

The volumes for beds in the stratigraphy older than 17 Ma were not calculated as the decompacted volume of the deeper seismic package is not well constrained.

Supplement 6

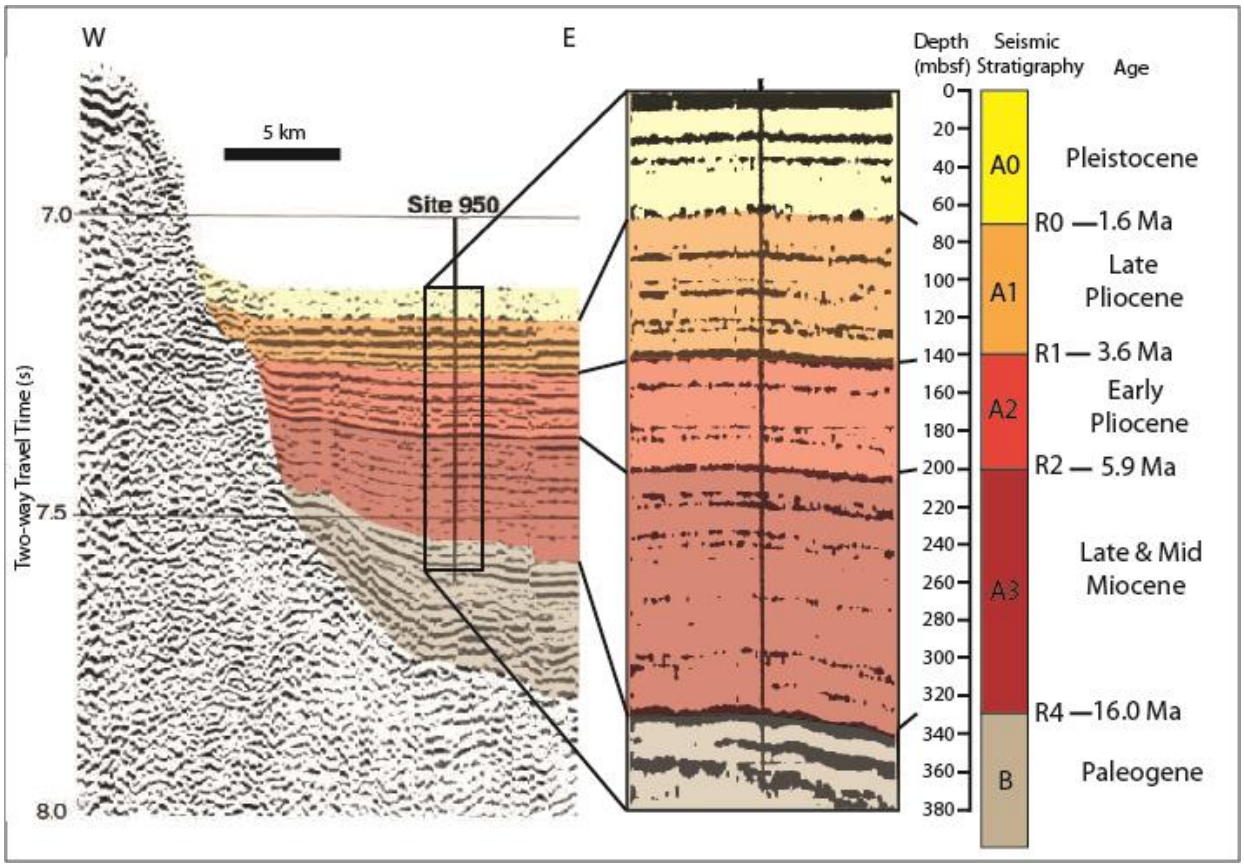

Supplement 6 | Seismic stratigraphy of the Madeira Abyssal Plain tied to ODP Core 950[7]. Data shows the simple layer-cake stratigraphy present that is used to generate single bed volumetrics based upon decompaction of single beds with seismic packages (Rothwell *et al*. 1998; Hunt *et al*. 2014; Hunt and Jarvis, 2017).

Supplement 7

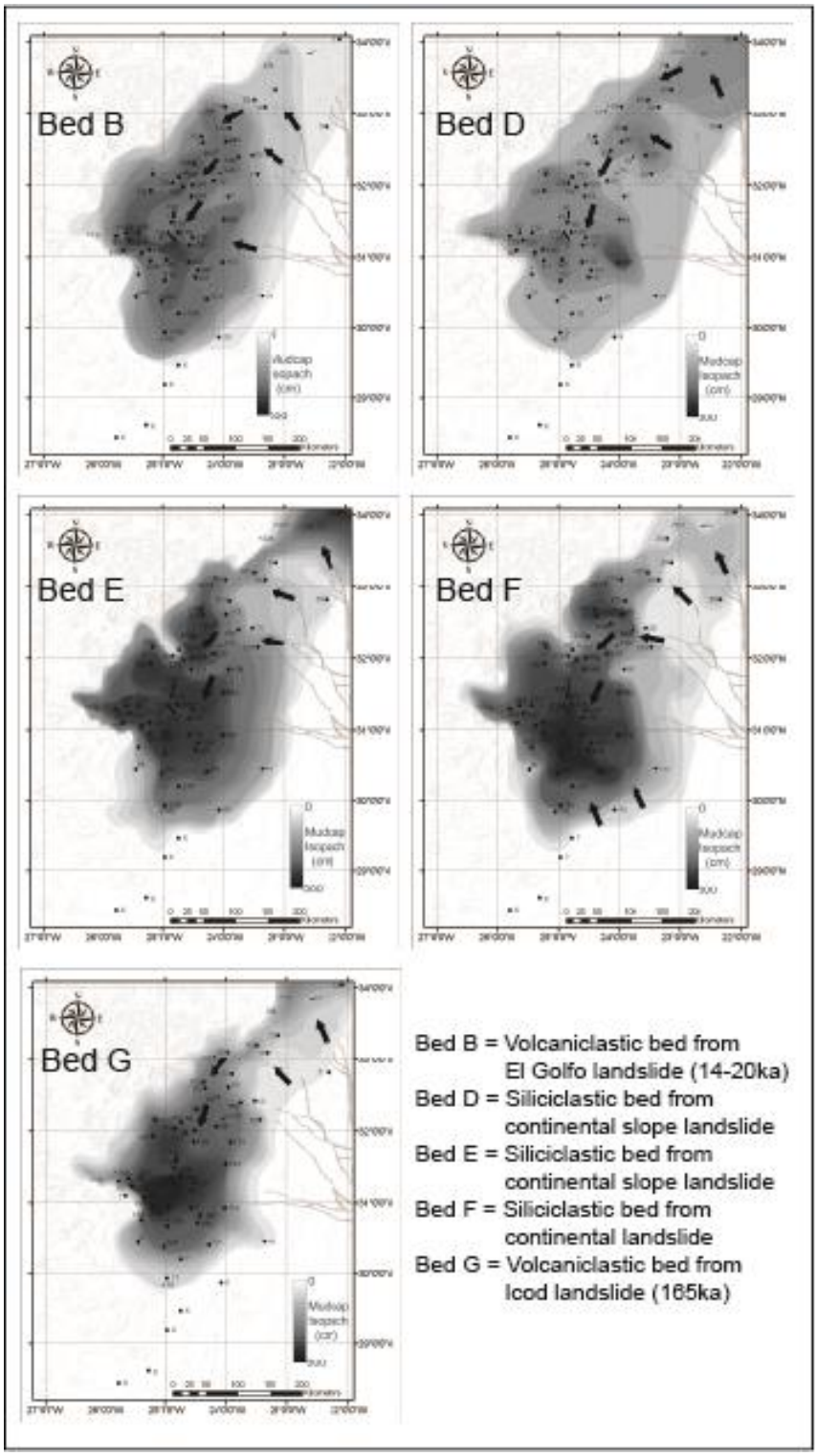

Supplement 7 | Isopach maps of Beds B, D, E, F and G in the Madeira Abyssal Plain based upon piston core coverage of the deposits. Data shows the thickness variations and limits of the deposits across the depocentres that can be used to constrain the deposit volumes.

Excel speadsheets:

Supplement 8 | Table of turbidite volumes of beds in the Madeira Abyssal Plain for deposits over the last 700 kyrs. Data shows complementary data used to report the volumes of these beds and how they compare to the volume estimates of the current study.

Supplement 9 | Table of turbidite volumes of calciclastic beds in the Madeira Abyssal Plain for deposits over the last 17 Myrs. Data shows the thicknesses of deposits at each ODP site and their conversion to decompacted volumes.